RESEARCH ARTICLE

Key Points:
- An alternative linear inverse formulation for kinematic source reconstruction is presented
- Such formulation can invert progressively growing data time windows while spanning the model space
- Promising advantages of this method are found, thanks to the preservation of causality and sparsity

Supporting Information:
- Supporting Information S1

Correspondence to:
H. S. Sánchez-Reyes,
hugo.sanchez-reyes@univ-grenoble-alpes.fr

Citation:
Sánchez-Reyes, H. S., Tago, J., Métivier, L., Cruz-Atienza, V. M., & Virieux, J. (2018). An evolutive linear kinematic source inversion. *Journal of Geophysical Research: Solid Earth*, 123. https://doi.org/10.1029/2017JB015388

An Evolutive Linear Kinematic Source Inversion

H. S. Sánchez-Reyes[1] [iD], **J. Tago[2], L. Métivier[1,3], V. M. Cruz-Atienza[4], and J. Virieux[5]** [iD]

[1]Institut des Sciences de la Terre (ISTerre), Universite Grenoble Alpes, CNRS, Saint-Martin-d'Heres, France, [2]Facultad de Ingeniería, Universidad Nacional Autónoma de México, Mexico City, Mexico, [3]Laboratoire Jean Kuntzmann (LJK), Universite Grenoble Alpes, CNRS, Saint-Martin-d'Heres, France, [4]Instituto de Geofísica, Universidad Nacional Autónoma de México, Mexico City, Mexico, [5]Institut des Sciences de la Terre (ISTerre), Universite Grenoble Alpes, Saint-Martin-d'Heres, France

Abstract We present a new hierarchical time kinematic source inversion method able to assimilate data traces through evolutive time windows. A linear time domain formulation relates the slip rate function and seismograms, preserving the positivity of this function and the causality when spanning the model space: taking benefit of the time-space sparsity of the rupture model evolution is as essential as considering the causality between rupture and each record delayed by the known propagator operator different for each station. This progressive approach, both on the data space and on the model space, does require mild assumptions on prior slip rate functions or preconditioning strategies on the slip rate local gradient estimations. These assumptions are based on simple physical expected rupture models we foresee. Successful applications of this method to a well-known benchmark (Source Inversion Validation Exercise 1) and to the recorded data of the 2016 Kumamoto mainshock ($M_w = 7.0$) illustrate the advantages of this alternative approach of a linear kinematic source inversion. This stabilized overparameterized optimization of a linear forward problem has a potential extension to stochastic inversion in a Bayesian framework in the future to assess uncertainties on kinematic source inversions, which is more difficult to investigate under nonlinear formulations.

Plain Language Summary In this paper we present a new method to infer the spatial and temporal history of an earthquake through the progressive analysis of seismograms that are not completely recorded at a given moment. Nowadays, the inference of an earthquake history is a common procedure that seismologists do after some minutes of the occurrence of an earthquake. The reconstruction of this history implies explaining many physical unknowns by interpreting the available seismograms. In this work we provide evidences that a progressive reconstruction is possible through the analysis of partially recorded seismograms. Furthermore, we find that the final reconstruction of such history appears to be better through the progressive analysis of seismograms than the results obtained with a traditional analysis of completely recorded seismograms.

1. Introduction

Nowadays, kinematic source parameters are routinely obtained for any moderate to large earthquake by geological services and research institutes around the world (e.g., the USGS in the United States or the NIED in Japan). Efforts have been made to develop fast and automated inverse methods (e.g., Diao et al., 2016; Hsieh et al., 2016; Ji et al., 2002) to provide a kinematic source model few minutes after an earthquake has occurred. However, for the reconstruction of the spatiotemporal distribution of the slip on a prescribed fault geometry, these approaches consider all available recorded data to be inverted altogether. In seismology, source modeling strategies preserving the causality could drastically take benefit of the natural time ordering of records. Moreover, assessing uncertainties on the estimated quantities is crucial as illustrated by the great variability of recovered slip models for recent earthquakes, such as Tohoku earthquake (Ide et al., 2011; Koper et al., 2011; Lay et al., 2011; Satake et al., 2013; Suzuki et al., 2011). In order to move toward imaging while recording as well as uncertainty quantification, a kinematic source inversion method based on a linear time-dependent formulation is a key ingredient for allowing progressive time windowing source analysis. The development of such a methodology is the purpose of this work.

In terms of data fitting, the kinematic source inversion is a procedure used to infer, from any set of seismological observations (seismograms, geodesy, ground motion recordings), a spatiotemporal representation of

the rupture history. This inverse problem can be stated as a least squares problem, where finding an optimal spatiotemporal slip rate distribution minimizing the differences between observed and computed data is the goal. However, the solution of this ill-posed inverse problem is nonunique (e.g., Cohee & Beroza, 1994; Cotton & Campillo, 1995; Hernandez et al., 1999; Minson et al., 2013; Wald & Heaton, 1994) and, according to current acquisition systems surrounding active faults, this problem is highly underdetermined in most cases, in spite of its rather simple formulation as a linear inverse problem.

Since Haskell, (1964, 1966) has promoted the idea of describing the seismic rupture as a finite sequence of breaking subevents, many strategies have been applied to solve this inverse problem. Ide (2007) provides a complete historical review on the evolution of these strategies. They can be divided into two main categories. On the one hand, we recognize those that are based on a linear inverse formulation linking linearly the spatiotemporal slip rate distribution as parameters and the synthetic seismograms predicting observations (e.g., Fan et al., 2014; Gallovic & Imperatori, 2014; Hartzell & Heaton, 1983; Wald et al., 1990). This linear formulation may lead to a significant number of parameters in the model space often composed of a 2-D fault surface and a time axis. On the other hand, model reduction strategies could be foreseen by prescribing a different parameterization driven by physical understanding of the seismic rupture process, such as slip rate direction, rupture velocity, rise time, and local maximum slip rate amplitude. The slip rate history is consequently a nonlinear function of these new parameters making the forward computation nonlinear (e.g., Cotton & Campillo, 1995; Hsieh et al., 2016; Ji et al., 2002; Liu & Archuleta, 2004). This inverse formulation with a significant reduction of unknown parameters greatly stabilizes the inversion procedure but prevents the simple use of linear algebra tools, especially for uncertainty quantification.

The ill-posedness of the problem while keeping a linear formulation requires dedicated strategies that are investigated in this work. For example, a progressive time windowing strategy introduces a data-driven hierarchy, illustrated nicely by previous studies of source deconvolution (Kikuchi & Kanamori, 1982, 1986, 1991). In addition to such strategy, model-driven regularization should be added while preserving the linear relation between model parameters and data. We propose a time domain kinematic source inversion strategy based on an adjoint-state method which honors causality and which preserves a linear inverse formulation as promoted by Fan et al. (2014) and Somala et al. (2014): this strategy acts as a deconvolution filter. Prior knowledge of the rupture and standard physically plausible regularization terms are key elements of this time domain implementation and can be efficiently introduced while still taking benefit of the causality of the seismic rupture. The related expansion of the model space, following the increase of recorded time, will introduce as well a way to stabilize the inversion while preserving the linear relation.

This article is organized in the following way. First, we introduce our kinematic source inversion technique. We present also a general strategy to include any type of prior information and regularization terms into the inversion scheme. It is then explained how to perform either a standard inversion of complete recordings or a progressive time window source inversion. Then, we illustrate the performance of the method by applying it to a well-known synthetic case (the Source Inversion Validation exercise 1 (SIV1) with a recent review by Mai et al., 2016). A real data application is presented for the 2016 Kumamoto earthquake which has already been studied by Uchide et al. (2016), Asano and Iwata (2016), and Hao et al. (2017). Finally, we provide a discussion on results, methodological perspectives, and numerical experiences gained during this work.

2. Methodological Description

We first intend to describe both the forward problem and the related misfit gradient computation needed for the inversion in the first part. We shall also describe how to consider model constraints for stable reconstructions. A more detailed explanation of the forward modeling based on integral approaches can be found inside the supporting information of this paper.

2.1. Background

In this work the following convention is used: nonunderlined symbols represent scalars, single underlined are vectors, and double underlined are matrices.

The source geometry is defined by a 2-D surface, $\Sigma(\underline{\xi})$, embedded in a 3-D known medium. Often, the fault position vector $\underline{\xi}$ is defined over a 2-D planar surface specified by strike ϕ and dip δ directions known prior to the rupture itself. Let us note that the formulation we shall describe could be performed for more complex

surfaces when needed: the normal vector may vary along the fault surface. A planar surface assumption is often a decent approximation with actual available data and it will simplify the notation. The forward problem is the computation of velocity recordings $\underline{v}(\underline{x}, t) = [v_x, v_y, v_z]^T$, at any receiver location $\underline{x} = [x_x, x_y, x_z]^T$ and time t during the interval $[t_1, t_2]$, given a certain spatiotemporal slip rate distribution $\underline{V}(\underline{\xi}, \tau) = [V_\phi, V_\delta]^T$, occurring at the position $\underline{\xi}$ and at a rupture time $\tau \in [\tau_1, \tau_2]$. For some applications, the instantaneous rake angle λ representing the slip rate direction at a given time and location on the fault can be predefined, reducing the 2-D $\underline{V}$ into a scalar value. A linear operator $\mathcal{P}_{ik}$ projects this slip rate sampling labeled by the 2-D or 1-D index k into a local 3-D Cartesian index i to be used when computing seismograms at receiver locations (Stein & Wysession, 2003) (see supporting information for further details). Thanks to the representation theorem and the reciprocity of Green functions, (Aki & Richards, 2002), the synthetic velocity field is computed as an integral over the source surface and the time window. This continuous representation of the forward problem

$$v_n(\underline{x}, t) = \int_{\tau_1}^{\tau_2} d\tau \iint_\Sigma \mathcal{P}_{ik} V_k(\underline{\xi}, \tau) \, \mathcal{T}_{in}(\underline{\xi}, t - \tau; \underline{x}, 0) d\Sigma(\underline{\xi}),$$

$$n, i \in [x, y, z] \text{ and } k \in \text{space}(\phi, \delta) \text{ or } k \in \text{space}(\lambda),$$

(1)

can be discretized and computed through the trapezoidal rule with a continuous trilinear interpolation in time and space of the slip rate function. In equation (1), the stress-state tensor $\underline{\mathcal{T}}$ is deduced from Green functions computed in the 3-D known medium. In this work, we assume double-couple sources with no opening mode during an earthquake. Therefore, the slip rate vector lies into a fault plane (at least locally).

Any method for computing $\underline{\mathcal{T}}$ is suitable, as long as tensor values could be stored at points on the source plane for each receiver as proposed by Zhao et al. (2006) and Hsieh et al. (2016). This off-line computation requires a sampling which should honor the physical description of the expected rupture front width and the wave propagation at the frequencies involved in the rupture reconstruction: if finer sampling is needed by the rupture physics, trilinear interpolation of these tensor components is often enough. These look-up tables are efficiently read and recovered when integrating the weighted slip rate function. They can describe any 3-D heterogeneous media as long as we know how to define these 3-D media. For instance, we have tested often used boundary integral equations (Perton et al., 2016) and sophisticated finite element methods (Tago et al., 2012) in our computational implementation with similar results when using the same medium definition. This precomputed and fixed wave propagation information will be of great importance for the progressive time windowing strategy because they will define the data window to be selected inside the current recorded window.

Let us now state the least squares problem we want to solve. The optimal spatiotemporal slip rate distribution will minimize the sum of squared differences between observed and synthetic time samples of seismograms. Synthetic seismograms are estimated through the discretized integral equation (1). The total misfit $C(\underline{V})$ is composed of a data misfit term and a model misfit decomposed in two terms as follows:

$$C(\underline{V}) = C_{\underline{d}}(\underline{V}) + \epsilon C_{\underline{m}}(\underline{V}),$$

(2)

where the hyperparameter ϵ will ease the global balance between the data and model terms of the gradient. This term could be absorbed into the definition of the model gradient, but the scaling between these two components is better controlled by this single parameter. The first term $C_{\underline{d}}$, known as the data misfit term, is given by

$$C_{\underline{d}}(\underline{V}) = \frac{1}{2} \sum_{\underline{x}} \int_{t_1}^{t_2} \left[\underline{v}(\underline{x}, t) - \underline{u}(\underline{x}, t)\right]^T \underline{\underline{W}}_{\underline{d}}^T \underline{\underline{W}}_{\underline{d}} \left[\underline{v}(\underline{x}, t) - \underline{u}(\underline{x}, t)\right] dt = \frac{1}{2} \sum_{\underline{x}} \left|\left|\underline{v} - \underline{u}\right|\right|_{\underline{\underline{W}}_{\underline{d}}}^2,$$

(3)

where the data weighting matrix $\underline{\underline{W}}_{\underline{d}}$ controls the contribution of each data residual ($\underline{v} - \underline{u}$). The upper script symbol T denotes the transpose matrix. In seismology, the data weighting matrix is often built as a diagonal matrix with a weight related to the noise for each trace, the epicentral distances or the azimuthal coverage. Recently, Hallo and Gallovič (2016) has proposed a way to incorporate into this data weight the missing knowledge of the medium propagation using uncorrelated uncertainties based on receiver-source distances

and azimuth coverage. In this work, we assume a diagonal shape of the matrix $\underline{\underline{W}}_d$ with values ranging from 0 (no contribution) to 1 (full normalized contribution), scaled by a normalizing factor related to the units of the data we use in order to get an adimensional misfit term as we are going to mix different quantities in the total misfit.

The second term of the misfit function is in charge of introducing in a least squares sense all available prior knowledge that we have in our hands, such as upper and lower expected rupture velocities, fault boundary slip penalization, expected shapes of the slip rate time functions, local rake angle variability, and others. This term requires two ingredients: a prior model $\underline{V}_p$ and a model weighting matrix $\underline{\underline{W}}_m$, giving us the following least squares expression:

$$C_m(\underline{V}) = \frac{1}{2} \int_{\tau_1}^{\tau_2} \iint_{\Sigma} \left[\underline{V}(\underline{\xi}, \tau) - \underline{V}_p(\underline{\xi}, \tau) \right]^T \underline{\underline{W}}_m^T \underline{\underline{W}}_m \left[\underline{V}(\underline{\xi}, \tau) - \underline{V}_p(\underline{\xi}, \tau) \right] d\Sigma(\underline{\xi}) d\tau. \qquad (4)$$

The prior model, $\underline{V}_p(\underline{\xi}, \tau)$, could be any preferential model of the spatiotemporal rupture history with a given hypocenter location, rupture time, rake angle, and shape of slip rate time functions: this model is often based on a simple physical description of the possible seismic rupture. The model weighting matrix $\underline{\underline{W}}_m$ is considered to be diagonal in this work, although nothing prevents us to define a band-diagonal structure for possible neighboring links in space and time. We leave it for future work. The design of these model ingredients must incorporate the following: (1) any desirable feature coming from seismic rupture models or other prior information of the event under investigation such as final surface displacements, attributes obtained from teleseismic phases or Global Positioning System measurements if they are not included in the data we invert and (2) the expected error between the running and prior models. This design will regularize the inverse problem by reducing the null-space size. We may add more than one model regularization term if different prior models have to be taken into account and the influence of such terms might vary during the inversion loop. This regularization term is in charge of emphasizing specific features of expected models. The design of the prior model and its weighting matrix is application dependent, and its construction will be further detailed at the description of the case studies investigated in sections 3 and 4.

We would like to highlight that, even if the design of this regularization term seems complex, having only one term flexible enough to include all the prior information available is very attractive. Furthermore, the design of this regularization term can be more physically meaningful if information coming from the geology, observed static displacements and/or previous studies can be translated into such prior model and its expected weight.

As for any inversion strategy with penalty/regularization terms, the adimensional hyperparameter ϵ balances the different terms contributing to the global misfit function. The choice of the amplitude of this hyperparameter has to be tuned according to a more or less arbitrary criterion, such as the L-curve analysis (Hansen, 1992) or by setting empirically this value through several trials in order to ensure that a decent data fit is performed. Another possibility is to previously calibrate this hyperparameter through several synthetic tests performed in a configuration similar to the real-case study where a known synthetic rupture has to be reconstructed.

Using equations (1), (3), and (4) we can formally state the kinematic source inversion problem as follows:

$$\min_{\underline{V}} \quad C(\underline{V}) = \frac{1}{2} \sum_{\underline{x}} \left|\left| \underline{v} - \underline{u} \right|\right|^2_{\underline{\underline{W}}_d} + \frac{\epsilon}{2} \left|\left| \left[\underline{V} - \underline{V}_p \right] \right|\right|^2_{\underline{\underline{W}}_m},$$

$$\text{s. t.} \quad F_n(\underline{v}, \underline{V}) = \int_{\tau_1}^{\tau_2} d\tau \int \int_{\underline{\xi}} \mathcal{P}_{ik} V_k(\underline{\xi}, \tau) \mathcal{T}_{in}(\underline{\xi}, t - \tau; \underline{x}, 0) d\underline{\xi} - v_n(\underline{x}, t) = 0, \qquad (5)$$

with the same index convention as for equation (1). It is worth mentioning that, because our forward problem is linear, the misfit function has a convex quadratic shape. Therefore, we can conclude that, for a given set of observed seismograms, there is only one optimal spatiotemporal slip rate distribution for which differences between observed and estimated seismograms is minimum. However, it is important to underline that, even with this formal existence of a unique optimal solution, the convergence might not be achieved for insufficient numbers of iterations depending on the shape of the misfit function. For some parameters with a rather

weak (if not null) imprint in the recorded data, we may never reach the convergence. Well-distributed observations, as well as a correct knowledge of the velocity-density structure of the medium, are essential but not enough: prior information on the slip rate model based on geological and physical understanding of the rupture process should be considered as well. As mentioned before, this inverse problem is ill posed and most of the time highly underdetermined, which makes the inclusion of regularization strategies a way to reduce the large null-space.

Finding the minimum of the misfit function leads to the following Newton equation:

$$\underline{\underline{\mathcal{H}}}_{C(\underline{V})} \underline{\Delta V} = -\underline{\mathcal{G}}_{C(\underline{V})} = -\nabla_{\underline{V}} C(\underline{V}), \tag{6}$$

where the matrix $\underline{\underline{\mathcal{H}}}_{C(\underline{V})}$ and the vector $\underline{\mathcal{G}}_{C(\underline{V})}$ (the n component is expressed as $\mathcal{G}_n(\underline{\xi}, \tau)$) represent the Hessian and the gradient of the misfit function. The model perturbation $\underline{\Delta V}$ will be added to the current model with a step length α^k estimated by the optimization procedure (Nocedal, 1980). The Hessian matrix is defined as second derivatives of the misfit function with respect to the slip rate parameters. Instead of estimating the Hessian matrix (slightly more computationally expensive), we rely on the estimation of the gradient which will be used in an iterative procedure for solving the Newton system (6). In this work, we use the limited-memory BFGS Broyden, Fletcher, Goldfarb, and Shanno (BFGS) quasi-Newton strategy (although steepest-descent or conjugate-gradient algorithms are possible with often more iterations; Nocedal, 1980). Consequently, the misfit gradient is the quantity we need to compute and its estimation is efficiently performed through an adjoint-state method (Plessix, 2006). Each gradient component of the misfit can be written as

$$\mathcal{G}_k(\underline{\xi}, \tau) = \sum_{\underline{x}} \int_{t_1}^{t_2} \mathrm{d}t \underline{\underline{W}}_d^T \underline{\underline{W}}_d \left[\hat{\underline{v}}(\underline{x}, t) - \underline{u}(\underline{x}, t) \right]_n \mathcal{T}_{ni}(\underline{\xi}, \tau - t; \underline{x}, 0) \mathcal{P}_{ik}^T$$
$$+ \epsilon \, \underline{\underline{W}}_m^T \underline{\underline{W}}_m \left[\hat{\underline{V}}(\underline{\xi}, \tau) - \underline{V}_p(\underline{\xi}, \tau) \right]_k, \tag{7}$$

with the same index convention as for equations (1) and (5). The first term in equation (7), which is the data term, is the sum of the projections of the unexplained residues at all the receivers onto the fault plane through the stress-state tensor, while the second term incorporates the prior model information. In reverse-time imaging as proposed by Fink (1993, 2008) and applied to earthquakes by Gajewski and Tessmer (2005), Ishii et al. (2007), and Larmat et al. (2006) among others, projections of observations (and not the unexplained data by the current model) are performed in the 3-D volume around the rupture zone or onto the 2-D rupture surface tracking the spatiotemporal evolution of the rupture front. This is the same difference between migration techniques and full waveform inversion in velocity model imaging where full observations are back-projected for migration while only unexplained observations are back-projected for full waveform inversion. We should highlight that the computational task of estimating the data misfit gradient and the model misfit gradient is quite simple, once the stress-state tensor has been precomputed and stored. Let us repeat that this tensor, which describes the influence of the velocity model, plays a quite important role in the reconstruction of the slip rate by inferring the causality due to propagation while preserving the linear formulation.

In this work, the 3-D space-time volume is sampled with a regular discretization along dip, strike, and time directions for the numerical estimation of the data gradient, although other discretizations are possible. Designing the discretization along these three directions is application dependent, and we shall consider here regular grids. The slip rate values should be evaluated at each node of the spatial grid and we assume a linear continuous interpolation of the slip rate over space. The regular time sampling is adapted to the frequency content of the data to be inverted. These samplings should honor the expected physical behavior of the slip rate function in space and time to be inverted which is more restrictive than the discretization related to the propagation.

2.2. Standard Inversion Strategy
The first strategy to reconstruct the time-space slip rate distribution which handles the complete available seismic data (from initial to final recording time) for a given event will now be introduced. Hereinafter we label this first strategy the Standard Inversion Strategy (SIS).

The algorithm (1), based on equations (1) and (7), provides the different steps necessary to perform the SIS which tentatively performs a simultaneous fitting of different wave packets recorded at the receivers: spatial/temporal leakage in the data gradient might occur as long as kinematic features of the data are fulfilled. Consequently, model gradient terms play a major role for modifying the descent direction and, therefore, stabilize the inversion.

1: **Specify** source geometry, $(\underline{\xi}, \tau)$, acquisition configuration, $(\underline{x}, t)$ and pre-computed stress-state tensor $\underline{\underline{\mathcal{T}}}$ from a velocity model (using any wave-propagator tool).
2: **Input** complete observations (3-component seismograms) at each receiver.
3: **Initialize** a zero slip-rate $\hat{\underline{V}}^k(\underline{\xi}, \tau) = \underline{0}$ for $k = 1$
4: **Design** prior model $\underline{V}_p$ and weighting matrix $\underline{\underline{W}}_m$.
5: **while** *Convergence is not reached (iterate over k)* **do**
   5.1: Compute $\hat{\underline{v}}^k(\underline{x}, t)$, forward modeling using $\hat{\underline{V}}^k(\underline{\xi}, \tau)$ in equation (1).
   5.2: Estimate residues, $\hat{\underline{v}}^k(\underline{x}, t) - \underline{u}(\underline{x}, t)$.
   5.3: Calculate gradient according to equation (7) and evaluate $\Delta\hat{\underline{V}}^k$.
   5.4: Update the slip-rate $\hat{\underline{V}}^{k+1} = \hat{\underline{V}}^k + \alpha^k\Delta\hat{\underline{V}}^k$, ($\alpha^k$ the step length).
end
     Algorithm 1: Standard kinematic source inversion strategy using the adjoint-state method.

2.3. Progressive Inversion Strategy

Instead of considering the entire data set, we may proceed in a hierarchical way taking benefit of causality by increasing the data time windows we consider through iterations. This sweeping strategy has often been used when imaging structures (Kolb et al., 1986). A data time-windowing strategy is expected to reduce the leakage related to time-space ambiguity, by taking benefit from sparsity and causality of this rupture problem (Heaton, 1990). The preservation of a time formulation is essential in this approach. We label this strategy the Progressive Inversion Strategy (PIS).

Observations in specific time windows defined for each receiver will be associated to a limited slip rate time-space zone. These data time windows are defined by the acquisition configuration with respect to the rupture surface and the velocity model described through the stress-state tensor between each point of the rupture surface and each receiver. For example, first recorded pulses are expected to come from the nucleation zone and they will impact nearest stations first. Therefore, stress-state tensors can be used for defining the data time window of each record participating to the rupture inversion assuming a simple expansion of the active zone inside which the expected slip rate should be.

Considering as known the hypocentral location, the origin time of the rupture and a maximum value of the rupture velocity, expected spatial zones, and time intervals, where the slip rate inversion is to be performed, can be specified through an Eikonal solver (e.g., Podvin & Lecomte, 1991). Using the precomputed stress-state tensors, it is possible to estimate the data time window at each receiver to be involved by these selected zones and intervals (Figure 1). Of course, these data time windows are specific to each receiver with the imprint of the propagation. For instance, a faraway station may have a different time window evolution compared to a near station. All expected phases should be included in these time windows, from the fastest *P* wave phases to the possible surface wave phases: this is why the *P* wave speed is used when solving the Eikonal equation.

Let us underline that these windows define a tight breakable region. Moreover, any time delay of converted phases is included in these time-dependent tensors, allowing a prediction of not-yet-recorded phases reducing the space-time leakage, thanks to the causality. However, in spite of this reduction of null-space size in this PIS, model gradient terms are still needed for better description of the rupture physics.
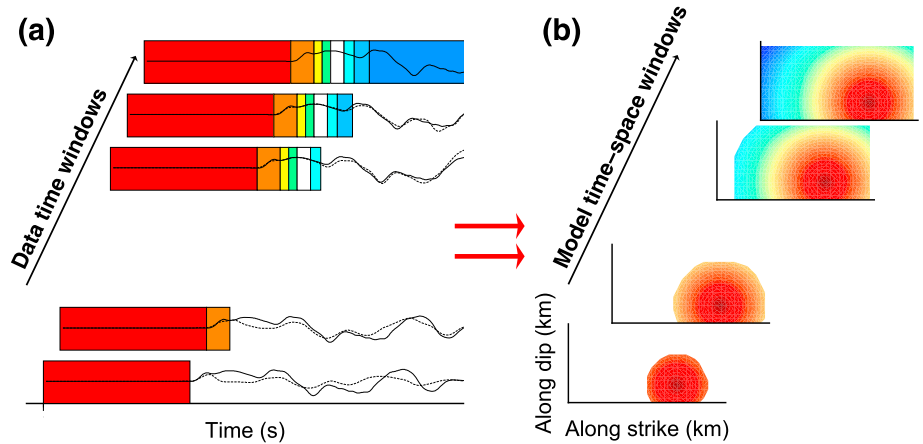
Figure 1. The illustrated selection of increasing data time windows is related to the temporal evolution of the seismic active zone. (a) Progressively increasing data time windows are highlighted with different colors after which the data is ignored during the current iteration of the inversion process. (b) Related active space regions increase with time. At a given time, only the active zone is allowed to be used for data inversion. The same colors, ranging from red to blue, are used for data and model windows in order to enhance their relationship. Notice that, at later stages of the PIS, only the residues between observations and synthetic recordings need to be explained: a key property of causality. Solid and dashed lines represent the observed and synthetic wave fields, respectively.

This strategy leads us to a slightly different algorithm compared to the previous one as described here

1: **Specify** source geometry, $(\underline{\xi}, \tau)$, acquisition definition, $(\underline{x}, t)$ and stress-state tensor $\underline{\underline{\mathcal{T}}}$.

2: **Input** first data time-windows at each receiver.

3: **Initialize** zero slip-rate $\underline{\hat{V}}^k(\underline{\xi}, \tau) = \underline{0}$, $k = 1$

4: **Design** prior model $\underline{V}_p$ and weighting matrix $\underline{\underline{W}}_m$.

5: **while** *Final data time-window is not reached* **do**

   5.1: Select the active fault zone and the time-window/receiver with the help of the $\underline{\underline{\mathcal{T}}}$.

   5.2: **while** *convergence is not reached (iterate over k* **do**

      5.2.1: Compute $\underline{\hat{v}}^k(\underline{x}, t)$, forward modeling using $\underline{\hat{V}}^k(\underline{\xi}, \tau)$ in equation (1).

      5.2.2: Estimate residues $\underline{\hat{v}}^k(\underline{x}, t) - \underline{u}(\underline{x}, t)$

      5.2.3: Calculate gradient according to equation (7) and evaluate $\underline{\Delta \hat{V}}^k$.

      5.2.4: Update slip-rate JOSUE SUGGESTS TO REMOVE THIS using Newton methods $\underline{\hat{V}}^{k+1} = \underline{\hat{V}}^k + \alpha^k \underline{\Delta \hat{V}}^k$, ($\alpha^k$ the step length).

  end

   end

     Algorithm 2: Progressive inversion strategy using the adjoint-state method for source imaging.

The interesting behavior of the PIS acting as a predictive deconvolution filter can be observed in Figure 1. Notice that, thanks to the wave propagation information stored in the stress-state tensors $\underline{\underline{\mathcal{T}}}$, a tentative prediction of the data recorded at time windows not yet considered at previous stages of the inversion process is already available from the time-space limited slip rate reconstruction. Therefore, as the time-space source active zone grows, the new parameters have to explain only the not-yet-understood residues related to the new data time windows. This progressive strategy mitigates the space-time ambiguity occurring in the SIS, thanks to the causality property of the time kinematic formulation.

2.4. Model Preconditioning

Besides the chosen strategy (SIS or PIS) and the regularization term, based on the model-driven gradient, we can apply a smoothing operator on the data gradient. The data-driven gradient is spatially filtered as $\underline{\mathcal{G}}^{new} = \underline{\underline{K}} \underline{\mathcal{G}}$, where the kernel $\underline{\underline{K}}$ represents a 2-D Gaussian spatial filter based on the corresponding correlation distances along-strike and along-dip directions of neighboring nodes. No time filtering is considered in this work. Such gradient smoothing does not require any hyperparameter setting but relies on the smoothing strategy driven by the expected features of the wanted model: this is why this smoothing is sometimes

called model preconditioning. This new smooth gradient is the one given to the optimization algorithm for updating the current model.

Because the acquisition is deployed at the free surface while the slip rate may vary with depth, a depth-dependent preconditioning is considered in this work, in a similar way for the compensation of illumination deficit with depth (Asnaashari et al., 2013; Pérez Solano, 2013; Plessix & Mulder, 2008). The new scaled version of the slip rate is

$$\hat{\underline{V}} = \frac{1}{z^c}\underline{V},\qquad(8)$$

where the local depth is denoted by z. Such model scaling turns the estimated gradient $\underline{\mathcal{G}}_n(\underline{\xi},\tau)$ from equation (7) into a new gradient

$$\hat{\underline{\mathcal{G}}}_n = z^c\underline{\mathcal{G}}_n,\qquad(9)$$

where a case-dependent constant c should be tuned. The values of this constant, as far as we have experienced, range from 0.01 to 1 in our different applications. Another strategy could be coarsening the grid while increasing the depth (Barnhart & Lohman, 2010): we prefer to keep the meshing simple in this work. Nevertheless, as in the case of the gradient filtering, this strategy is case-dependent and a previous calibration of constant c has to be conducted on synthetic exercises before performing any inversion of real data.

3. Synthetic Case: Source Inversion Validation Exercise 1

Before a possible application to real data, the verification of both approaches is essential. Thanks to a research community effort recently reviewed by Mai et al. (2016), different examples are proposed for the validation step. The Source Inversion Validation exercise 1, named SIV1, is considered here for which both behaviors of misfit-data term and misfit-model term will be investigated as we know the model solution. Let us underline that the velocity model is assumed to be perfectly known for this synthetic case and all observations are noise-free: an optimistic point of view when considering real data. In other words, we are in a very favorable situation for this synthetic analysis and the obtained solutions would be the optimal ones for the undertaken approaches in real cases.

3.1. SIV1 Description

In the SIV1, the source geometry is a fault plane with known strike $\phi = 90°$, dip $\delta = 80°$, and rake $\lambda = 180°$ (Figure 2b). The fault is embedded in an elastic layered isotropic medium (Figure 2a). The dimensions of the fault are approximately 35 km along strike by 20 km along dip. The final slip, slip rate time histories, and rupture speed are heterogeneous along the fault (Figures 2c and 2d). As prior information, the location of the hypocenter, the final seismic moment ($M_0 = 1.06 \times 10^{19}$ N m, $M_w = 6.69$), and the fact that the rupture does not reach the surface (see Mai et al., 2016 for details) are input information aside seismograms. Forty receivers at the surface with three-component noise-free velocity recordings (maximum resolved frequency about ≈ 2.5 Hz) are available in the distributed database. As it can be seen in Figure 2b, the 40 receivers formed a satisfactory azimuthal coverage.

3.2. Settings: Discretization, Regularization Design, and Preconditioning Strategies

Four scenarios are presented with different SIS workflows. The first one, referred as SIS1, carries a SIS without any regularization term or prior information. The second case, which will be called SIS2, applies the regularization and preconditioning strategies just described previously. For these first two cases, we allow the rake angle to smoothly vary inside the interval [150°–210°]. Two additional exercises, SIS1* and SIS2*, are considered where exactly the same configuration is used as for the first two exercises, but the rake angle is kept to its exact value ($\lambda = 180°$) during the inversion.

As mentioned earlier, the 3-D (strike, dip, and time) slip rate model space must be discretized for accurate forward modeling on one side and for feasible inversion using a limited number of degrees of freedom. The time discretization is related to the frequency content of the data. A maximum frequency of 1 Hz is considered for this synthetic exercise. Therefore, a time sampling of the slip rate time-space history Δt of 0.25 s corresponds to half of the Nyquist sampling. The spatial discretization is controlled by two characteristic lengths. The first
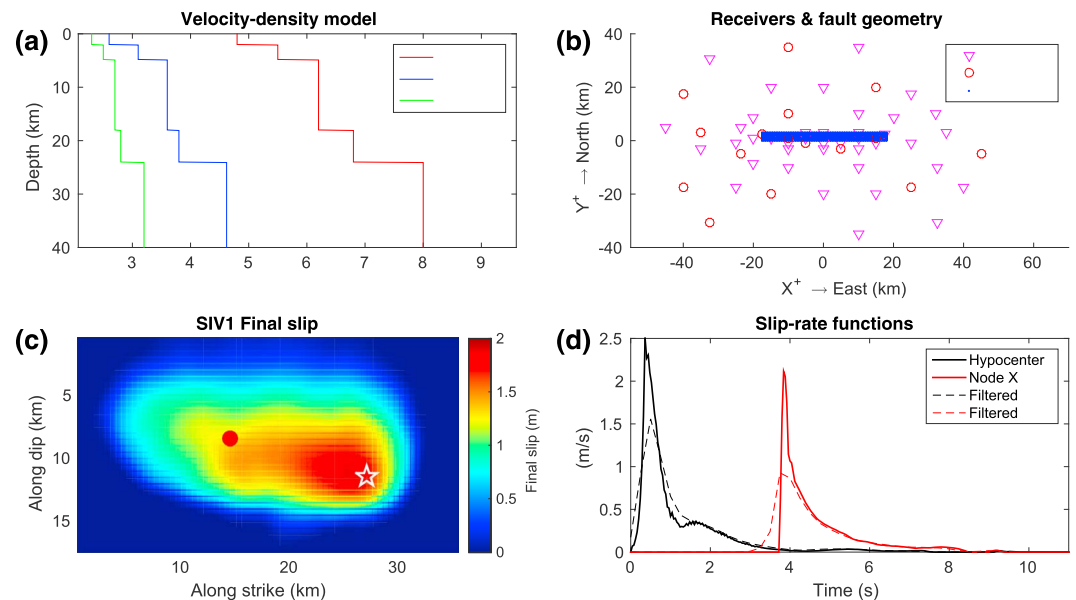
Figure 2. Summarized description of the SIV1. (a) Velocity-density structure of the embedding medium. (b) Surface projection of the fault geometry (2,592 fault odes) and the locations of the 40 receivers used for the inversion (40 I. Sta) and 16 used to verify the predicted velocity recordings of the inversion results (16 P. Sta). (c) Final slip distribution along the fault after ≈10 s of rupture. (d) Slip rate time functions from two different locations, at the hypocenter (black line) and far from it (red line). The slip rate functions are from the positions represented by the star and the circle at (c). Dashed lines on panel (d) represent the slip rate functions of the filtered version of the SIV1 (0–1 Hz) used in this work. Information taken from Mai et al. (2016).

one is related to the Green function and related wave propagation. The grid spacing must be a small fraction of the shortest expected wavelength, which turns out to be shorter than 1.3 km for a minimum shear velocity V_s of 2.6 km/s. The second characteristic length is related to the rupture front width. The rupture front width depends on the rise time and the rupture velocity. The spatial spacing has to sample enough the rupture front width for a continuous propagation of the rupture front. The rupture front width can be roughly estimated by multiplying the mean value of the expected rupture speed and the rise time. Thus, by considering a mean rise time of 4 s and a rupture velocity of 70% of the minimum V_s, the rupture front width will be around 7.3 km. Consequently, a spatial discretization Δx sampling of 1 km in both the strike and dip directions is selected. The choice of the discretization is crucial for the inversion: the total number of invertible parameters can be a drastic way to control sizes of the model space and the null-space.

Taking into account this discretization setting, we set our synthetic exercises as follows. The duration of observed seismograms is 35 s for all of 120 traces with a maximum frequency of 1 Hz. For real earthquakes, the maximum frequency of the observations used for source inversion are usually lower (e.g., frequency bands between 0.025–0.25 Hz and 0.025–0.5 Hz). High-frequency content is sensitive to small-size heterogeneities of the medium velocity, already difficult to include in the propagation, preventing reconstruction of the corresponding slip rate contribution for the source at these frequencies. In this exercise, the medium is exactly known but our restriction to 1 Hz might represent a more realistic situation. In order to speed up the time convolution, we decimate signals down to a sampling rate of 0.1 s, representing 87% of the original data set. Let us highlight that the slip rate time-space history and the observed wavefields have different time sampling rates (0.25 s versus 0.1 s) but an equal frequency content up to 1 Hz. The fault geometry is represented through 36 × 18 nodes equally separated every 1 km along strike and dip, respectively, for correct rendering of the continuous forward problem. The total duration of the rupture is fixed to last less than 9.5 s. Therefore, the total number of parameters describing the slip rate distribution for the first two cases is 36 [nodes along strike] × 18 [nodes along dip] × 39 [time samples] × 2 [slip rate components] = 50,544 when the rake angle is unknown, and half this amount 25,272 when the rake angle is fixed to a given value. In contrast, the total number of observations in both cases is 141 [time samples] × 120 [traces] = 16,920. For coherent comparison, the time-space discretization is the same for all exercises. Each of the inversion strategies has a different stopping criteria related to the time window that they invert. For the exercises where the SIS is applied,

the stopping criterion is set to a limited number of iterations (20 maximum) or a convergence tolerance equal to a normalized misfit less than 1×10^{-2} related to the initial total data misfit $C_d(\underline{V})$. On the other hand, the stopping criterion for each stage of the PIS is set so that at least a certain number of iterations is performed (10 maximum) and a convergence tolerance equal to a normalized misfit less than 1×10^{-2} related to the data misfit of only the data time window that is taken into account at that stage is ensured. These two criteria are defined in this way in order to avoid overfitting the data when performing a large number of iterations.

The prior model, $\underline{V}_p$, and weighting matrix, $\underline{\underline{W}}_m$, are incorporating the following information. The prior model is built as a rupture which starts at the known hypocentral location. The rupture front of this prior model propagates at the local shear wave velocity at the beginning of the propagation and it slows down while it goes far from the hypocenter (Figure 3a). The rupture times are computed through an Eikonal solver (Podvin & Lecomte, 1991) and an additional delay (ranging from 0 s to 0.5 s) is added to the calculated rupture times according to a Laplacian function in terms of the correlation distance between the different nodes in the mesh and the hypocenter location. Yoffe-type functions (Tinti et al., 2005) with 5 s of effective rise time and 0.5 s of duration of the positive acceleration are assumed. The total slip amplitude is fixed to 1.6 m at the nodes inside a central region of the fault plane and it decays exponentially while approaching the borders of the fault geometry.

The weighting matrix $\underline{\underline{W}}_m$ is designed to emphasize to which extent model prior information is trustful. Because the prior information ensures that the rupture does not reach the surface, strong weights are given to the slip rate difference $\underline{V} - \underline{V}_p$ at shallow nodes and at those nearby the other boundaries of the predefined fault. Slip rates at those nodes are set to zero initially and, therefore, any nonzero slip rate is strongly penalized at these nodes. At the same time, the weighting matrix can also penalize any slip rate values occurring at lower or higher rupture speed than the expected limits. For these exercises, the model weighting matrix is designed in such a way that ruptures propagating faster than 1.4 times the local shear wave velocity (V_s) are strongly penalized (i.e., rupture time upper limit). To prevent that a node breaks a second time or to limit the energy at that node after an expected duration of the rupture, we also include a lower limit that penalizes any rupture happening at a given node after 5 s beyond the passing time rupture at that node. Figures 3b and 3c offer a comparison between slip rate distribution to be reconstructed (uppermost panels), the designed prior model (second uppermost panels), and the evolution of these highly penalized areas (third uppermost panels) on the fault at different times of the rupture. The weighting matrix is constructed based on an expected area of confidence around the prior model. At each node, the time history of the confidence grows linearly from the first expected rupture arrival and another rupture arrival propagating at V_s. Then, the confidence decays as a Gaussian curve the half width of which lasts the expected duration of the slip rate functions (5 s). This weighting matrix is related to physically meaningful model covariance and the global hyperparameter ϵ scales the model misfit with respect to the data misfit: this is the reason why this scaling is not integrated into the weighting matrix for making explicit this balance between data and model terms.

Let us note that the prior model is designed in such a way that information about the minimum and maximum rupture speeds, vanishing slip at the fault boundaries, and expected rake angle limitations are included. Fast changes from low to high values during the time evolution of the weighting matrix represent the limits on the expected rupture velocities (Figure 3b). Moreover, the Yoffe-type slip rate functions of this prior model are chosen in order to see if the inverted slip rate functions could benefit from this prior information on the shape of the time history (Tinti et al., 2005). A comparison between target and prior model slip rate functions, at a node far from the hypocenter, is provided in Figures 3b and 3c. A prior homogeneous final slip of 1.6 m is allowed uniformly over the breakable zone, giving equal probable contribution everywhere inside this zone. The panels of Figure 3 illustrate these constraints on the possible rupture process.

When regularization is activated, the depth-dependent model preconditioning and the data gradient smoothing strategies are also applied. For the depth-dependent strategy we found that, for this receiver configuration, the optimal value of the constant c is ≈ 0.08. In addition, a 2-D Gaussian-shaped filter with correlation distances of 3 km and 2 km along strike and dip, respectively, is applied to the data gradient at each iteration of the inversion to ensure the spatial coherence of the slip rate distribution.
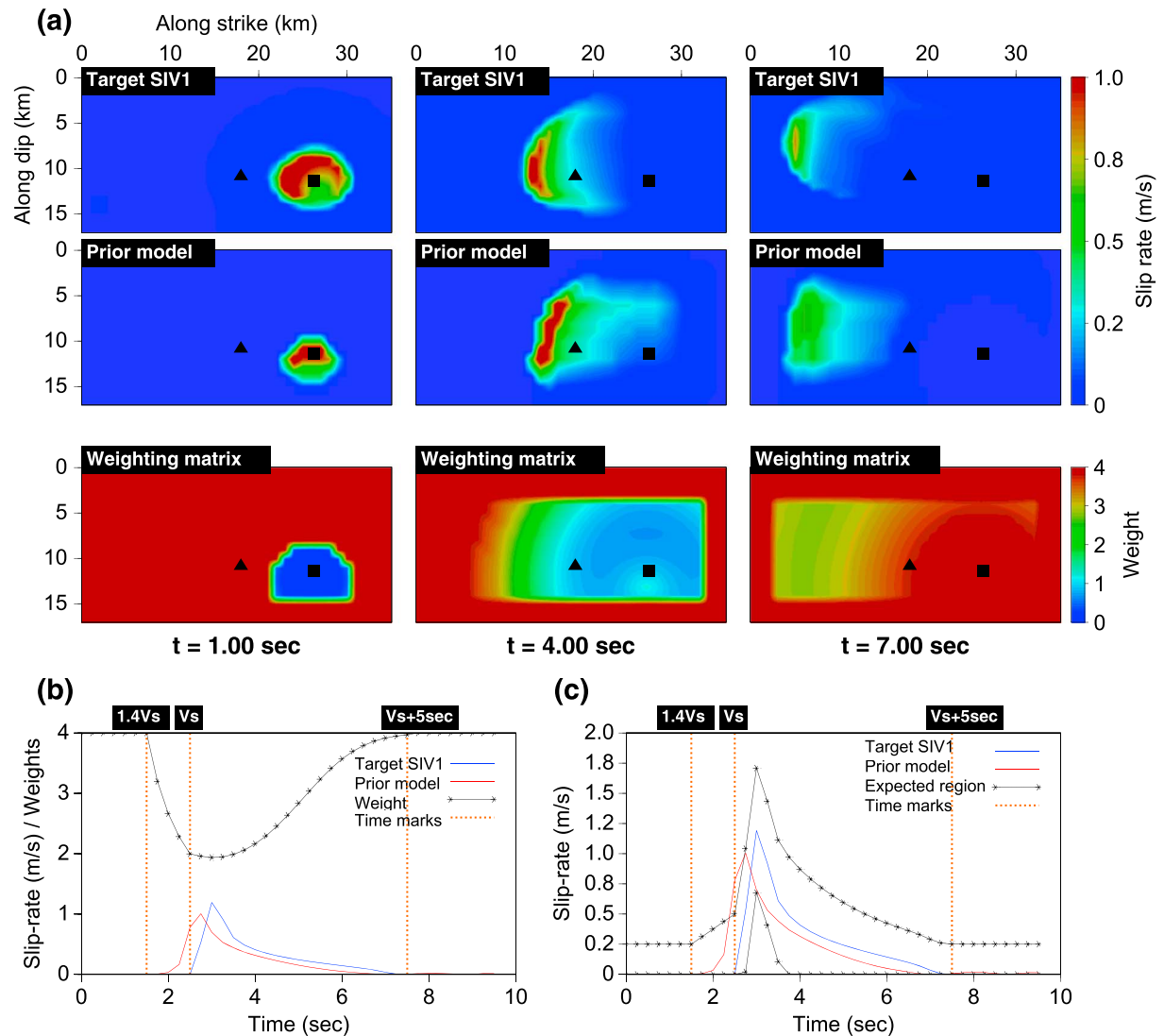
Figure 3. Summary of the designed prior model, $\underline{V}_p$, and weighting matrix, $\underline{\underline{W}}_m$. (a) Illustration of the time evolution along the fault of the filtered version of the SIV1, the prior model and its associated weighting matrix at 1, 4, and 7 s of rupture (from left to right). Panels (b) and (c) show exactly the same comparison of the amplitude of the slip rate functions from the filtered version of the SIV1 (blue line), the prior model (red line), and the weight time history (black line on b). On panel (c), the weight time history from panel (b) is translated into the expected zone where the rupture is preferred (black line on c). Time marks (orange dashed lines) on (b) and (c) illustrate the arrival times of rupture fronts propagating at speeds of $1.4V_s$ (rupture time upper limit) and V_s as well as the expected rise time (5 s, rupture time lower limit). The location of the fault node at which slip rate functions and weight time history are shown on (b) and (c) is represented by a black triangle on panel (a), while the hypocenter is represented by a black square. In the representation of the weighting matrices shown at the bottom of panel (a), the confidence on the prior model is represented by the colors ranging from blue (low confidence) to red (high confidence).

3.3. SIS Synthetic Case

Figure 4 and Table 1 summarize the results for these four exercises by comparing their final data misfit, model misfit (resolved slip rate functions versus filtered version of the SIV1), mean value, and standard deviation of the rake angle extracted from the solutions and estimated seismic moment.

As expected, when no prior information is used (except the hard limits of the expected rake angle range), time-space ambiguity will impact the fitting of the observations. As a consequence, results for the SIS1 show slip everywhere on the fault (Figure 4a). The configuration of SIS1 allows to correctly minimize both data and model misfit but the results are worse than for the other cases. Even without regularization, one may notice that the reconstruction is significantly improved when keeping fixed the rake angle (SIS1*). The improved results from the SIS1* correspond to the reduction of the number of invertible parameters when assuming a known rake direction instead of performing a vectorial reconstruction of the slip rate (Figure 4c).
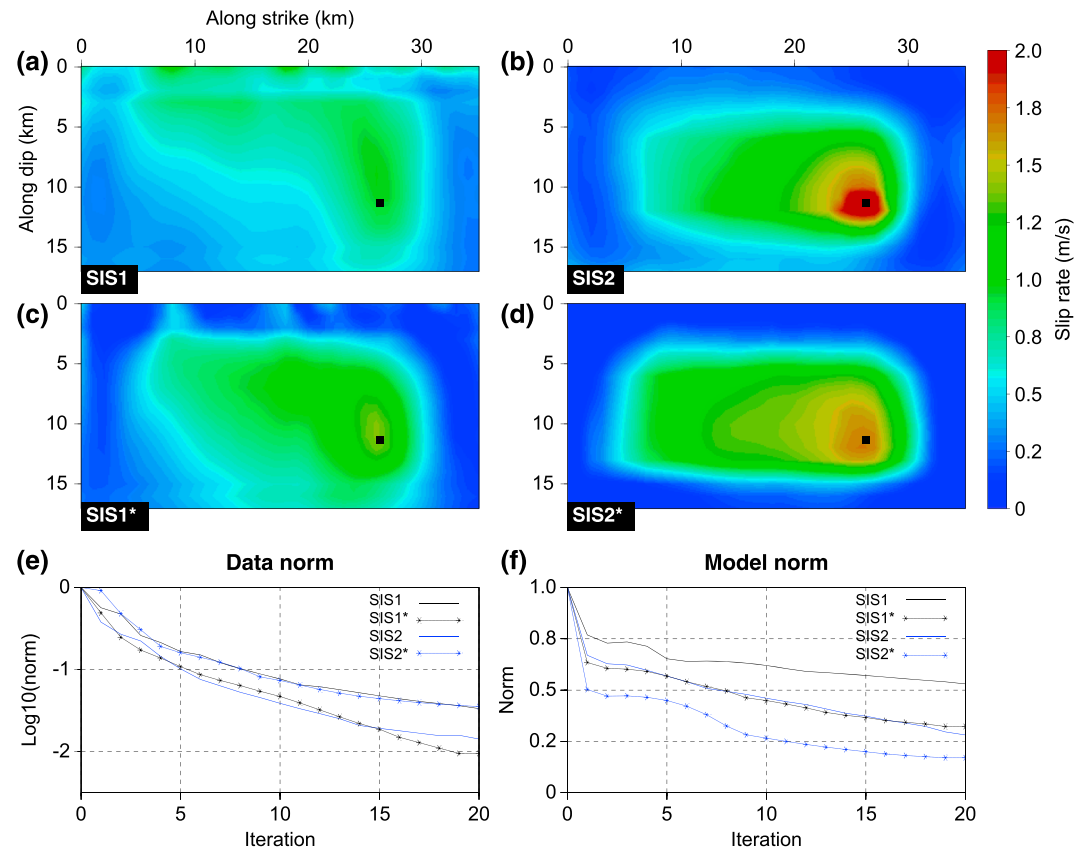
Figure 4. Comparison of the final slip resulting from applying the SIS with and without regularization. Results from panels (a) and (b) are obtained without assuming any rake angle (allowed to vary between 150° and 210°). Panel (a) comes from a SIS without regularization or preconditioning and (b) includes regularization and preconditioning. Panels (c) and (d) show the results from the SIS when the rake angle is fixed to its correct value ($\lambda = 180°$. Panel (c) is obtained without regularization or preconditioning, while panel (d) is obtained with regularization and preconditioning. Panels (e) and (f) illustrate the evolution of the data and model L2 misfit norm through the iterative process of inversion, respectively.

However, according to Figure 4f, when regularization is included without strong rake constraints (case SIS2, Figure 4b) the reduction of the model misfit shows comparable results to the nonregularized and fixed rake exercise (case SIS1*, Figure 4c). Therefore, in terms of model misfit, fixing the rake at the correct value allows an improvement comparable to the one gained when prior information is used to regularize the inversion for this synthetic exercise. Even though cases SIS1 and SIS2 overestimate the final seismic moment (Table 1), they underestimate the local final slip and slip rate amplitudes almost everywhere, which is another consequence of the spread of the information onto a large number of parameters. Regularization terms help to decrease this time-space leakage but results are not significantly improved.

Contrary to these poor final slip estimations and slip rate reconstructions, the exercises without fixing rake values (SIS1 and SIS2) provide a satisfactory estimation of the average rake angle (Table 1). Fixing the rake by considering only the slip rate modulus as the inverted parameter is essential for reducing the number of parameters and for a significant improvement of the slip rate reconstruction. Following this idea, a hierarchical two-step inversion scheme, where an initial inversion is performed first to infer the local rake direction of the sliding and where a second inversion with fixed rake direction inverts for the slip rate amplitude, can be a very useful strategy. A preliminary estimation of these local directions will allow us not to oversimplify the rupture history: smooth variations of local rake angles seem to be a reasonable assumption as we do not expect drastic changes of the sliding direction in less than 1 km distance. Such two-step strategy will be of great importance when tackling real data sets. In realistic conditions, few prior information on spatial variations of the rake is available, acquisition systems are not dense enough to properly illuminate the fault and the limited knowledge of the velocity medium make even more challenging the rake angle recovery.

Table 1
Summary of the Results for the SIS and PIS Cases Applied to the Filtered SIV1

	$M_0 \times 10^{19}$ (N m)	Data misfit (%)	Model misfit (%)	Mean $\lambda \pm \sigma_\lambda$ (deg)
SIV1-filtered	1.052			180
SIS1	1.157	3.35	53.02	186.47 $\pm$ 20.61
SIS2	1.225	1.42	28.16	181.73 $\pm$ 9.08
SIS1*	1.153	0.95	32.28	180
SIS2*	1.174	3.54	17.03	180
PIS1	1.175	1.52	40.68	182.66 $\pm$ 8.59
PIS2	1.128	1.03	30.34	181.31 $\pm$ 3.23
PIS1*	1.103	0.34	22.68	180
PIS2*	1.053	0.18	13.83	180

Results from cases SIS1* and SIS2* (Figures 4c and 4d) illustrate the importance of prior information on the rake angle. When this information is available (e.g., from focal mechanisms deduced from teleseismic phases), the inversion is able to better locate and estimate the zone of maximum slip. Even when no regularization (except the assumed fixed rake angle) is used in case SIS1*, the cross talk between nodes decreases and the estimated maximum slip (1.4 m) reached 80% of the expected value (1.8 m). However, the exercise SIS1* still shows relevant slip (0.6–0.8 m) at the deepest boundary. Therefore, additional regularization and preconditioning play a complementary role for the exercise SIS2*. Results from this exercise are the best among these four exercises: the zone of maximum slip is well located and its amplitude (1.7 m) is very close to the expected one. For the case SIS2*, the whole final slip is less overestimated than for the other three exercises and the regularization term and preconditioning strategies partially remove the slip at regions where rupture is not expected to happen. Let us underline that, without imposing any direct constraint on the seismic moment, the computed M_0 for SIS2* overestimates by 11% the true value. However, results from SIS2* required various prior information: rake angle bounds first through a vectorial reconstruction and then by keeping it fixed, hypocenter location, free-surface vanishing slip coming from potential geological observations, and expected expansion of the slip rate surface with time.

In general, we observe that the space-time ambiguity between nodes is strongly reduced when the information of the rake is used. When regularization terms are used, both data and model misfits improve. The prior model regularization term removes exactly what is expected: slip vanishes at boundaries of the predefined geometry, slip rate does not occur before the time of the predefined rupture time at each position and may not restart after an expected duration if not requested by the data. As a consequence, the final slip estimation over the whole fault is better predicted. Let us now perform the same four exercises using the PIS.

3.4. PIS Synthetic Case

The following four exercises preserve the same time-space discretization, regularization configuration and preconditioning strategies of the exercises described in the previous section: we simply substitute the acronym PIS instead of SIS, meaning that an evolutive selection of the data is going to be inverted. Exercises PIS1 and PIS2 are the two-component inversion where the rake angle is allowed to smoothly vary between 150° and 210°. In the same way as before, PIS1* and PIS2* are exercises where the rake angle is fixed ($\lambda = 180°$). These labels PIS2 and PIS2* refer to exercises where the prior information regularization term and the depth-dependent model preconditioning and the data gradient smoothing are applied.

The main difference between the SIS and PIS strategies is related to the data we use at each stage of the inversion procedure. Different progressive time windows are defined for mapping a limited time-space region of the source into a limited window of seismic signals. For the PIS, one has to specify these time windows to consider at each receiver for the specific time-space source zone to be imaged. Therefore, a preliminary procedure has to be carried out to define these time windows. By using an Eikonal solver (Podvin & Lecomte, 1991), we define a concentric rupture zone starting from the hypocenter until the edges of the predefined fault geometry with an expected maximum rupture speed of 1.4 times the local shear wave. Such overestimation of the rupture speed prevents the concentration of energy at the hard upper limits of the allowed time-space zone where the rupture is allowed to occur and admits possible supershear ruptures. From these specific rupture times at each node of the fault, we define a synthetic rupture scenario by placing the beginning
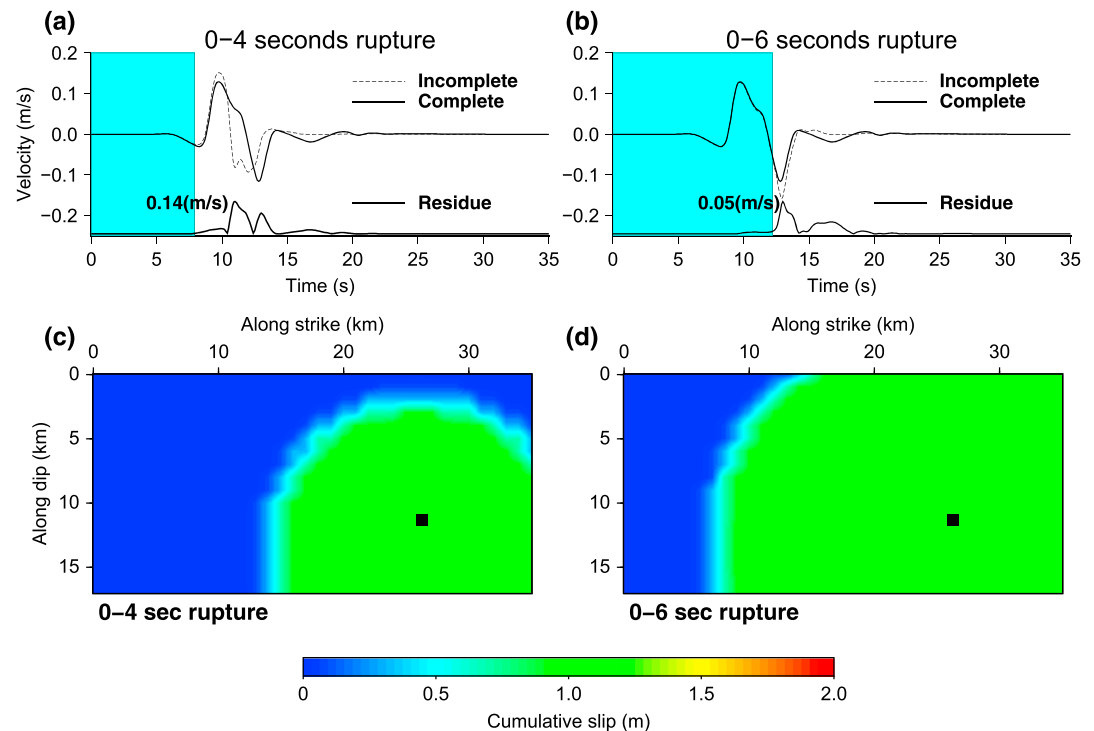
Figure 5. Progressively increasing data time windows for each component at each station can be determined through the analysis of residues between complete and incomplete seismograms. On panels (c) and (d), the cumulative slip for different time-space intervals of a synthetic rupture is shown. The analysis of the residues between complete (recorded after the whole rupture of 9 s, solid black line) and incomplete recordings [for 4 s, and 6 s, dashed lines on (a) and (b)] define the blue time window to be used during the PIS. The absolute residual value is plotted below traces in a different scale where the maximum value is written next to it. The black square on panels (c) and (d) represents the hypocenter location.

of generic-shape slip rate functions at the correct rupture time for each node. Contrary to the rupture times estimated through the Eikonal solver, the shape and duration of the slip rate functions of this synthetic rupture scenario are not crucial to correctly define the time windows for each stage of the inversion. However, we recognize that the effective rise time of these generic-shape slip rate functions has to be close to the expected duration (4–5 s). An example of a concentric synthetic rupture with Gaussian-shape slip rate functions and a homogeneous final slip of 2 m is illustrated in Figures 5c and 5d. Using this synthetic rupture scenario, a direct forward modeling is performed to compute synthetic seismograms at all receiver locations. Then, we consider several progressively increasing rupture time-space zones and their corresponding incomplete seismograms computed at all receiver locations to define these time windows specific to each receiver. By analyzing residual differences between complete and incomplete seismograms for each progressive time-space zone, we can detect the time after which residues are negligible, giving the final time we must consider for each rupture window. Figures 5a and 5b illustrate this time-hashing procedure.

As Figures 5a and 5b show, the wave propagation information from the precomputed stress-state tensor allows a rough prediction of the time windows not yet considered according to the analysis of the residues for a given inversion stage. As the source time-space region allowed to break spans, the incomplete prediction gets closer to the observed recording and the data time windows extend faster. Therefore, regardless of the receiver location, the data time windows are shorter at the beginning and their duration increases rapidly. We should mention as well that, because the inversion of the first data time windows already provides a given prediction of the unexplained data, the following inversion stages need to explain only residues inside the new data time windows as for iterative deconvolution (Kikuchi & Kanamori, 1991). The evolution of the misfit function is completely different from the SIS, because the data size is varying through stages. For the following exercises, nine time-space zones of the synthetic rupture are considered: they are (i.e., 0–1.0, 0–1.5, 0–2.0, 0–2.5, 0–3.5, 0–5.0, 0–7.0, 0–9.0, and 0–10.0 s).
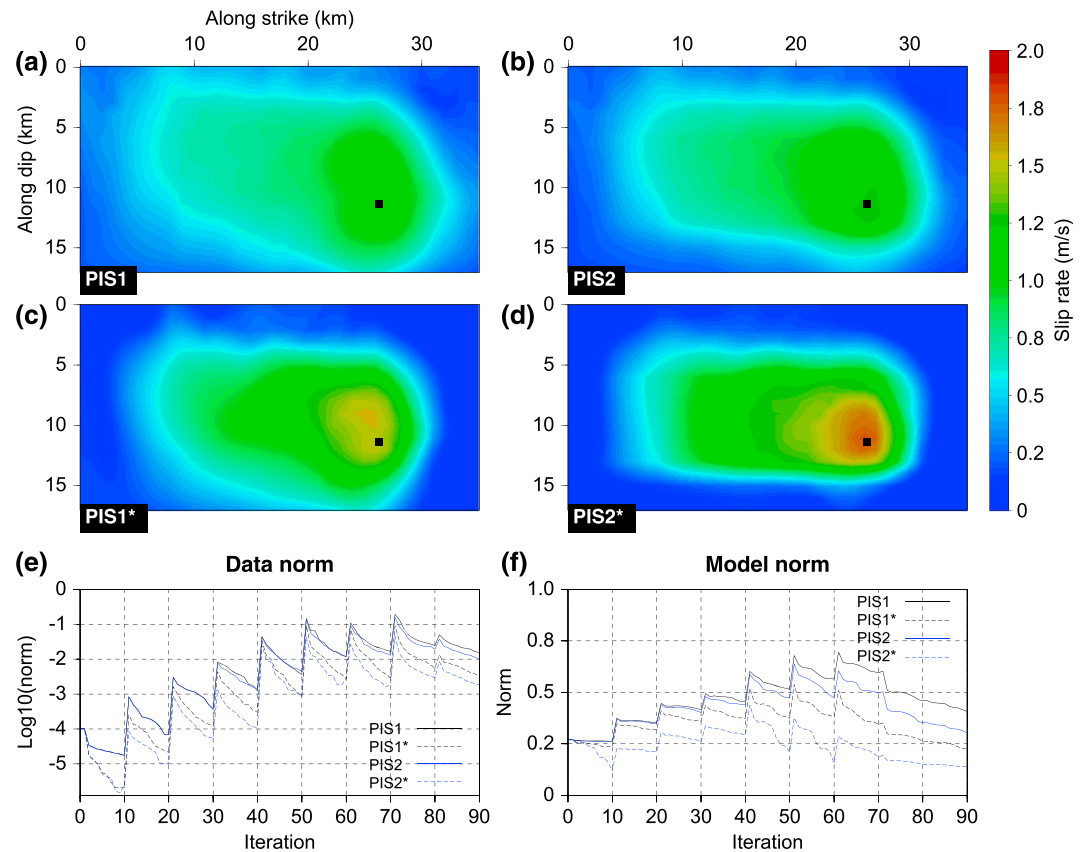
Figure 6. Same exercises as Figure 4 but applying the PIS. Results from panels (a) and (b) come from inversions that do not assume any rake angle (allowed to vary between 150 and 210°). Panels (b) and (a) are obtained from the PIS with and without regularization and preconditioning strategies, respectively. Panels (c) and (d) show the results from applying the PIS when the rake angle is kept fixed ($\lambda = 180°$). Panel (c) does not consider any regularization while panel (d) applies regularization and preconditioning. Panels (e) and (f) illustrate the evolution of the data and model L2 misfit norm through the iterative process of inversion, respectively.

Finally, in order to better enforce causality into the prior information, results from every previous stage of the progressive inversion are used for updating the prior model $\underline{V}_p$ and the model weighting matrix $\underline{\underline{W}}_m$. The evolving prior model is built as a hybrid of the previous results and the initial prior model. Therefore, the slip rate time functions from the initial prior model at the nodes that were inside the previously allowed source region are replaced by the reconstructed solution from the previous stage, while the functions at the nodes outside this area are kept from the initial prior model. An additional 2-D spatial smoothing (the same as the one applied to the gradient) has to be applied over the new hybrid prior model to avoid discontinuities. In order to ensure that the information from the following data time windows do not affect considerably the results from previous inversion stages (i.e., to respect causality), the weighting matrix is also changed so that any difference between the current model and the hybrid prior model will be strongly penalized at the zones where the prior slip rate functions were already replaced. We may highlight that this simple way of modifying and freezing the prior information is completely based on the causality of the phenomenon. In addition, this evolutive prior information prevents a strong influence of the prior model in the final reconstruction. In fact, this strategy reduces the impact of the initial prior model in such a way that we have to increase around 100% the value of the hyperparameter ϵ at each new inversion stage.

Once the data time windows are defined, the progressive inversions for the four exercises follows the algorithm (2). Due to the progressive build up of parameters and data time windows, the computational time of one iteration of the progressive inverse process at early stages is shorter ($\approx$0.3 s) than an iteration assuming the final number of parameters to invert ($\approx$2 s). Stopping criteria are those mentioned before for proper comparison between previous exercises.
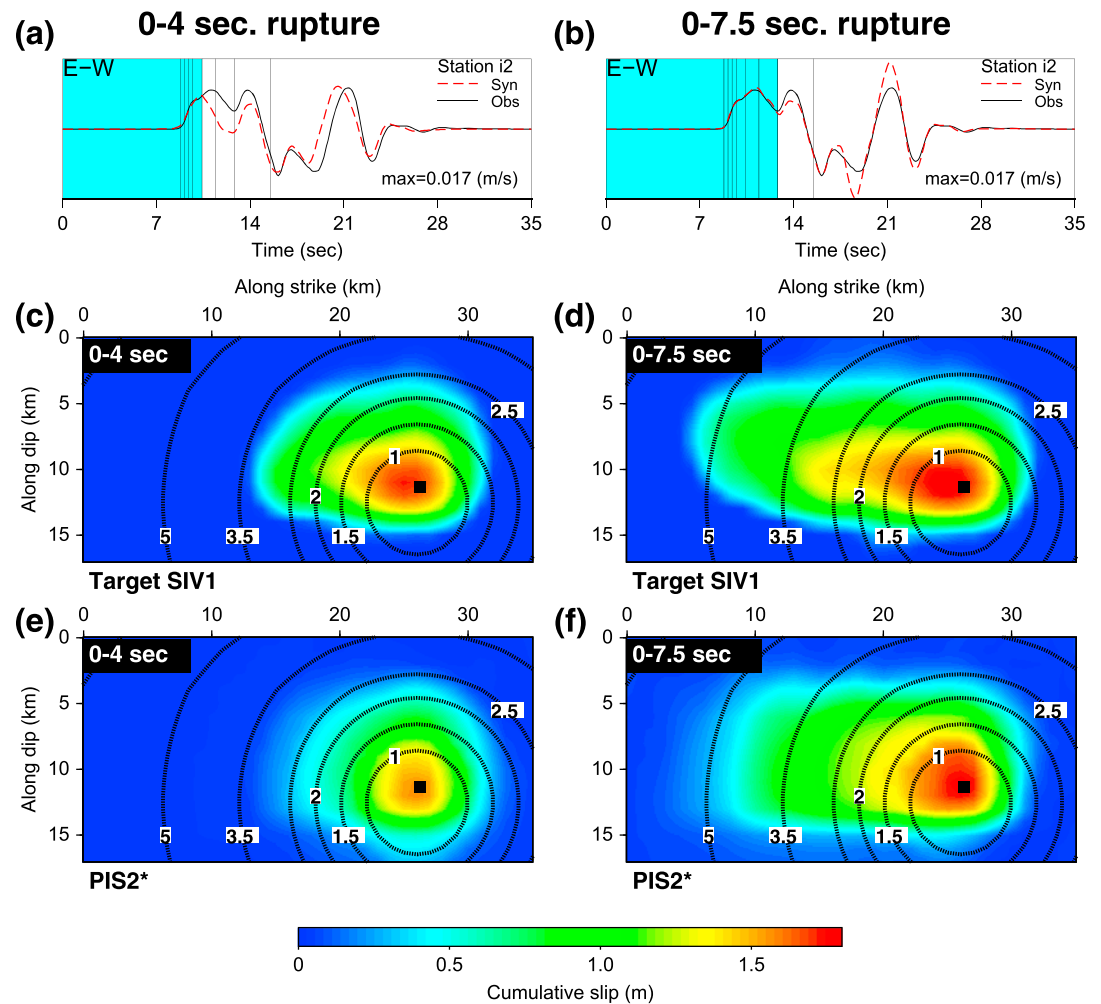
Figure 7. Comparison between cumulative slip distributions coming from the filtered version of the SIV1, panels (c) and (d), and the ones obtained from the PIS2*, in panels (e) and (f), which are obtained for the inversion of two different limited data time windows illustrated in panels (a) and (b). Panels (a) and (b) show two different data time windows used (blue-colored window) at receiver location "i2" (see Figure 2b) to invert for the slip rate time-space history for time intervals of 0–4 s and 0–7.5 s. Notice that by inverting a small amount of data (blue-colored data windows), we are able to predict waveforms that have not yet been used (data outside the colored windows) because they have been delayed by the propagation. Dashed black lines overlaying the slip distributions illustrate the increasing allowed 2-D area where the rupture is allowed to happen at every time interval (0–1, 0–1.5, 0–2.0, 0–2.5, 0–3.5, 0–5.0, 0–7.0, 0–9.0 s). Vertical black lines in panels (a) and (b) represent the time limit of the data time windows for each stage of the PIS.

The results from these four exercises applying the PIS without and with regularization terms are summarized in Figure 6 and Table 1. Let us remind that the rake angle is always constrained in a limited range when both slip rate components are inverted.

Compared to the results from the previous section, all the four PIS exercises fit better the data than their SIS counterparts. The saw shape of both misfit functions (Figures 6e and 6f) can be explained by the growth of the data records and the model parameters every time that new data have to be explained. We also recognize that cases PIS1 and PIS2 are able to better estimate the rake angle than the cases SIS1 and SIS2, as well as the seismic moment (Table 1). The PIS1 gets closer to the solution than its counterpart SIS1, decreasing its model misfit by 13% (see Figures 6f and 4f and Table 1). However, we do not see this amount of improvement of the data and model misfits when comparing PIS2 to SIS2. The better seismic moment estimation comes from a mitigation of the time-space ambiguity. When a SIS is carried out, even with regularization, the inversion is allowed to place values of the slip rate at any time and at any place to enforce a better misfit reduction, which ends up with the overestimation of the seismic moment. The improvement of the seismic moment estimation
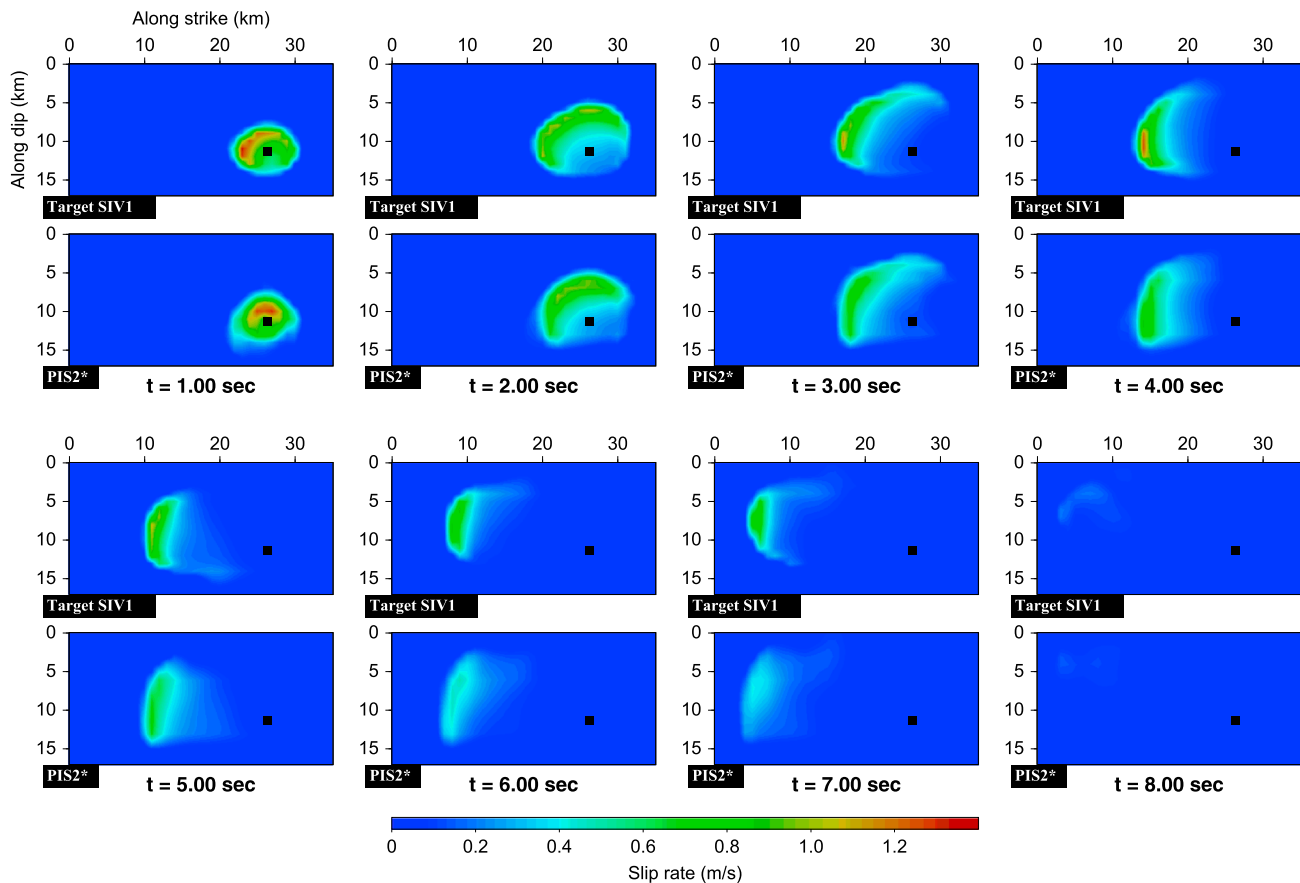
Figure 8. Comparison between the filtered version of the SIV1 (0–1 Hz) and the resulting slip rate spatiotemporal distribution obtained from the PIS2*. For each snapshot, the corresponding rupture time is shown at the bottom of each snapshot couple.

and the better rake reconstruction can be quite useful for real-earthquake applications for which the lack of information about local rake angles and the overestimation of the seismic moment are recurrent problems.

The results from exercises where the rake angle is fixed are also closer to the solution than their SIS counterparts. Compared to SIS1*, the results from PIS1* improved ≈10% in terms of model misfit, while the data misfit is decreased by a factor 3. Improvements are even more significant for the last exercise PIS2* that is the closest to the solution and to the observed data according to the misfits (Table 1). Furthermore, looking at the evolution of the data and model misfit of the PIS2* (Figures 6e and 6f) we recognize that, even at its maximum values, the progressive reconstruction of the slip rate time-space history is never very far from the solution (43% model misfit) and the observed data time window (4.5% data misfit). We interpret this feature as a correct progressive reconstruction of the rupture history.

Summarizing the results from the PIS exercises, we could say that in general they fit better the data. The progressive introduction of the data allows an improved rake recovery, avoiding leakages of parameter values between space-time nodes. Moreover, restricting the zone of reconstruction of the slip rate and freezing the previous results through the evolutive prior model expresses the causality feature between the slip rate and the seismogram: phases coming from a specific zone of the source surface may arrive as energy packets with different propagation times at stations, leading to a natural hierarchy in the inversion procedure. Signals beyond the current inverted data window are already explained by the current active fault zone: only residues should be interpreted at the next stage, preventing the leakage to the next active zone, reducing drastically the spatial spread of information. An illustration of this important feature is presented in Figure 7, where the cumulative slip estimated from the partially reconstructed solutions inverted from shorter data time windows (0–4 and 0–7 s) are shown as well as the predicted unrecorded data.
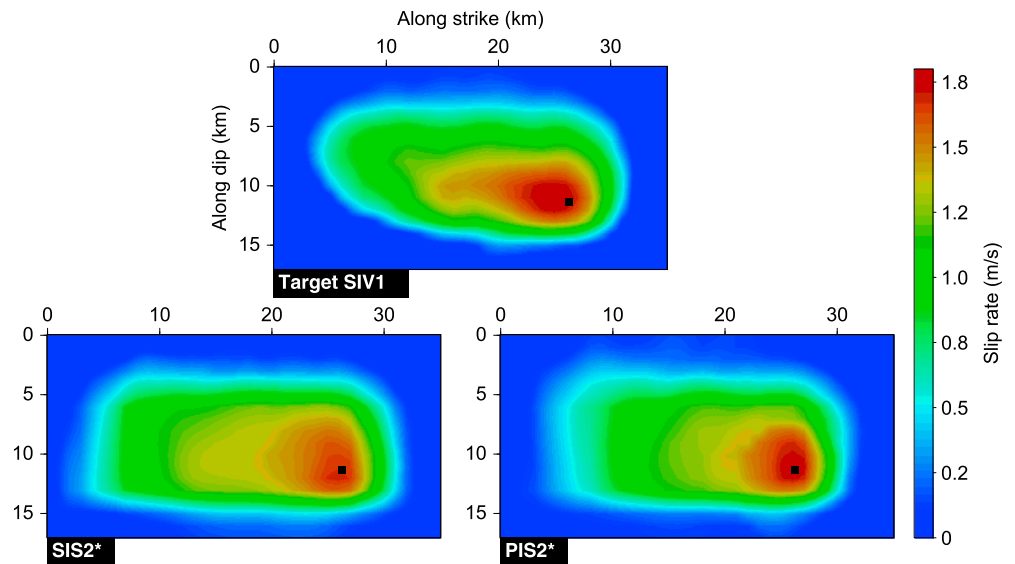
Figure 9. Final slip comparison between the filtered version of the SIV1 (0–1 Hz) and the solutions for the cases SIS2* (bottom left) and PIS2* (bottom right). While these two results achieve comparable final data and model misfit, the PIS2* shows a better along-strike final slip distribution. Both inversion results shifted the maximum slip zone by ≈1 km along dip direction.

The time evolution of the reconstructed slip rate time-space history from our best approach (exercise PIS2*) is shown in Figure 8. The reconstructed slip rate shows an overall underestimation compared to the true model. However, we recognize that such underestimation gets worse when the rupture front goes far from the hypocenter (snapshots at $t = 6.00$, $t = 7.00$, and $t = 8.00$ s in Figure 8). In general, the time-space leakage of the solution is much less near the hypocenter and the origin time, thanks to the reduced number of parameters involved at earlier stages of the progressive inversion. When the progressive inversion tries to solve for nodes far away from the hypocenter, the time-space leakage increases because more parameters are considered, as for the SIS case. This is also true at the end of the rupture time history.

As a partial conclusion, Figure 9 provides a final comparison between the best results from the SIS and PIS workflows, both applying regularization and preconditioning strategies. Results form the PIS2* spread less across the fault than the ones from the SIS2*, counterbalanced by the time evolution. In both cases, the zone of maximum slip is correctly located. However, the PIS2* case seems to have a better along-strike and along-dip behavior. The improved behavior of PIS2* can be seen as well in Table (1) comparing data and model misfit as well as the estimated seismic moment. The SIS2* fits the target solution almost as well as the PIS2* (17% versus 13%), but the data misfit is 19 times larger than the one from the PIS2* (3.54% versus 0.18%) and the seismic moment is more overestimated (11.6% versus 0.1%).

The results from both strategies are satisfactory. However, we prefer the PIS2* case, because poor acquisition design and less accurate velocity model could favor the PIS workflow, which is expected to be more robust by reducing the number of involved parameters at each inversion step. Moreover, as it is illustrated in Figure 7, this strategy opens the door to quasi-real-time implementations and assimilation techniques for uncertainty estimation that are not considered here.

4. Real Case: 2016 Kumamoto Earthquake

4.1. Description

These two inversion strategies are applied to the main shock of the 2016 Kumamoto earthquake sequence. This event occurred at 16:25:05.47 UTC on 15 April 2016 according to the National Research Institute for Earth Science and Disaster Resilience (NIED). As reported by Uchide et al. (2016) and Asano and Iwata (2016), this event has activated slips along two different fault segments of the Futagawa and Hinagu fault systems in the Kumamoto prefecture, Southwest Japan (Figure 10a). Both fault systems exhibit a dextral strike-slip motion (Uchide et al., 2016). The velocity structure used to precompute the stress-state tensor is taken from the results of a regional travel time tomography presented by Uchide et al. (2016), and the values of the density for each
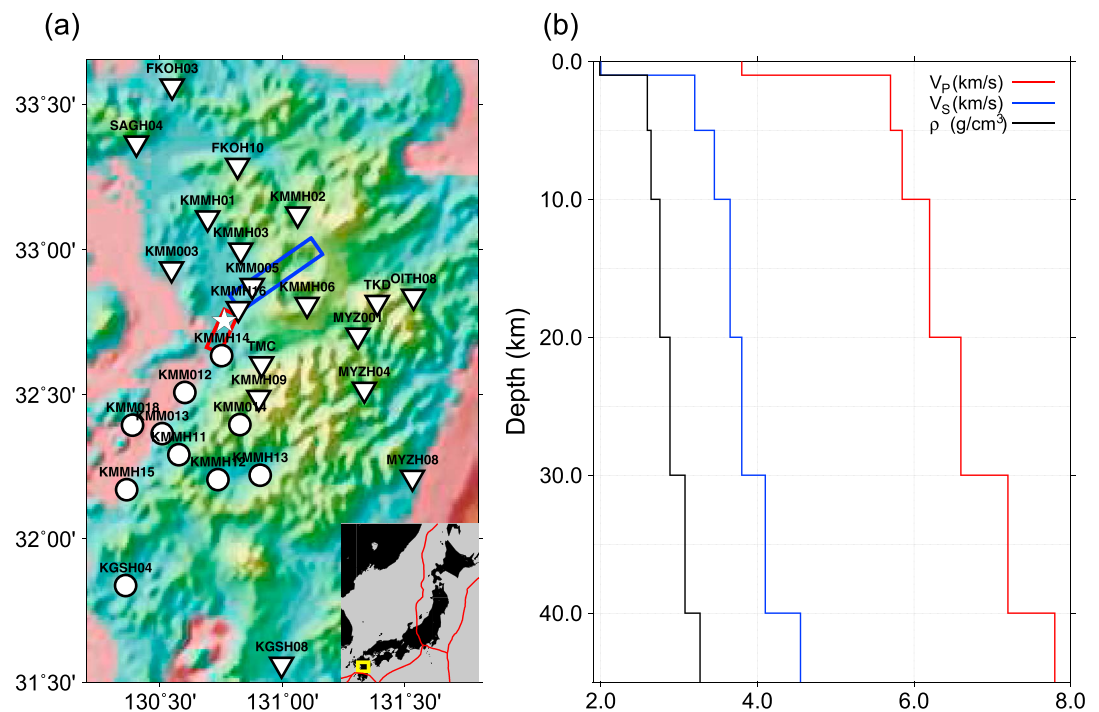
Figure 10. (a) Fault geometry and location of receivers recording the 2016 Kumamoto earthquake (M_w 7.0). The rectangles indicate the surface projection of the Futagawa (blue) and Hinagu (red) fault segments assumed in this work, while the white star represents the epicenter reported by the NIED. Inverted triangles are used to illustrate the location of the 19 receivers used in the inversion, while the 11 circles represent locations where waveforms are just predicted. (b) Velocity-density structure used to estimate the stress-state tensor. The velocity model was taken from Uchide et al. (2016) and the density was derived from the linear relationship between V_P and ρ presented by Berteussen (1977).

layer are estimated by assuming a linear relationship between V_p and ρ taken from Berteussen, (1977; see Figure 10b and Table 2).

Two 3-component velocimeters from the Broadband Seismograph Network (F-net) and 28 three-component accelerometers from the strong-motion seismograph Networks (K-NET and KiK-net) have recorded this event at epicentral distances shorter than 150 km. Not all recordings are used in the following inversion exercises, mainly due to the complexity of the recordings related to evident site effects at certain locations. For the K-NET and KiK-net networks, recorded accelerograms are converted from counts to acceleration, baseline corrected and integrated to particle velocity recordings. For the F-net network, the velocity recordings are deconvolved by the instrument response and baseline corrected. Then, all velocity recordings are band-pass filtered inside the window [0.025–0.25] Hz by applying a one-pass butterworth of first order. Anticausal zero-phase filters were not used as the main idea behind the PIS is to benefit from causality. However, we do not see large differences in the inversion results when zero-phase filters are applied.

We adopt the fault plane geometry from Asano and Iwata (2016) with a longer length along the strike direction: this longer dimension is in better agreement with the geometry used by Uchide et al. (2016; Table 2 and Figure 10). The fault geometries from these two authors were built according to the aftershock distribution and the surface trace of known active faults. Their main difference is less than 5° for strike and dip angles. Segment lengths differ as well: we prefer longer fault segments to avoid the nonphysical accumulation of slip at the boundaries.

4.2. Settings: Discretization, Regularization Design, and Preconditioning Strategies
The total fault surface is discretized in 290 nodes equally spaced every 2 km along-strike and along-dip directions. This space discretization is in agreement with the maximum observed frequency of 0.25 Hz. We are able to detect minimal rupture durations of 4 s: the rupture speed is expected to be between 2.6 and 2.2 km/s. The duration of the rupture will last less than 20 s. The time sampling rate of the slip rate functions is set to 0.5 s, which is 4 times shorter than the maximum sampling rate allowed according to the highest frequency limit of the observations (0.25 Hz). Observations are decimated to have samples every 0.1 s with a duration

Table 2
Kumamoto Fault Geometry and Velocity-Density Structure Used in This Work (Modified From Uchide et al., 2016)

	First segment	Second segment	Depth (km)	V_P (km/s)	V_S (km/s)	ρ (g/cm^3)
	Hinagu	Futagawa				
Strike (ϕ)	205°	235°	0–1	3.80	2.00	1.98
Dip (δ)	72°	65°	1–5	5.70	3.20	2.59
Rake (λ)	180°	210°	5–10	5.85	3.45	2.64
σ_λ	±30°	±30°	10–20	6.20	3.65	2.75
Length (km)	18	40	20–30	6.60	3.80	2.88
Width (km)	20	20	30–40	7.20	4.10	3.07
Nodes	90	200	40–	7.80	4.55	3.26

of 65 s. The number of parameters involved in the inversion is 41 [time samples] × 290 [fault nodes] × 1 [slip rate component] = 11,890, as we assume the rake angle as known from prior information, while the number of observations is 30 [receivers] × 3 [components] × 131 [time samples] = 11,790. However, only 19 stations out of the 30 available are considered in the inversion, which decreases the number of observations to 19 [receivers] × 3 [components] × 131 [time samples] = 7,461. The other remaining 11 stations are not used for the inversion due to their complexity. However, we provide a comparison between these complex recordings and the synthetic waveforms predicted from our best reconstruction of the slip rate distribution.

For this real case, we consider two different exercises. The first one, labeled as SIS-KUMA, assumes prior information on the rake angle to fix the relationship between the two components of the slip rate vector. This prior information is obtained from the previous results reported by Asano and Iwata (2016). Regularization based on a prior rupture model as well as the depth-dependent and smoothing preconditioning strategies are also included for SIS-KUMA case. The second exercise, labeled PIS-KUMA, applies the PIS to exactly the same configuration of the SIS-KUMA case. PIS-KUMA and SIS-KUMA strategies differ only on the way the data are provided to the inversion scheme and the related evolution of the regularization term during the progressive inversion.

The prior model used in both cases is built based on the slip time-space evolution of the inversion results from Asano and Iwata (2016): a general suggestion when considering building a kinematic source scenario. This slip evolution is estimated by the commonly used multiple time window linear waveform inversion method (Hartzell & Heaton, 1983; Olson & Apsel, 1982). This solution, freely available on the Web from Asano and Iwata (2016), is interpreted in terms of the slip rate evolution, needed for our formulation. The whole time-space slip history is built up, based on the reported amplitude of the basis functions (smooth ramps) corresponding to each time window at every subfault. The time-space slip history is then interpolated in time and space over a finer grid and smoothed in order to reduce the effects of the discretization. The slip rate distribution is then obtained through the time derivative of the reconstructed smoothed version of the slip evolution. Finally, the information at the location of the assumed geometry for this work is extracted from the reconstructed slip rate history. Figure 11 illustrates the final slip and the reconstructed slip rate time history across the assumed fault geometry.

The diagonal model weighting matrix $\underline{\underline{W}}_m$ is designed according to the expected confidence we have on the prior model. Any slip occurring at the deepest and the two along-dip boundaries of the fault geometry are strongly penalized (Figure 11a, bottom). The upper limit of the rupture velocity is set to 1.2 times the local shear wave speed, while the lower limit is set in such a way that the rupture at each node is promoted to have rise times of ≈5 s. The estimation of the rupture times, necessary to build the weighting matrix, is carried out through the previously used 2-D Eikonal solver (Podvin & Lecomte, 1991). Figure 11a (bottom) illustrates as well that the weighting matrix allows to define a time-space region where the slip rate is expected to occur. As in the synthetic case, we give a high confidence to the prior model at regions where the slip rate is prevented to happen (i.e., at early or latter rupture times) and a lower one where the rupture front is expected to be. In this way we incorporate in a flexible way all the prior information related to rupture velocity, amplitude, and shape of the slip rate function. The solution might go beyond these limits when asked by the data content.

For each of the following exercises, the hyperparameter ϵ is set in different ways. For the SIS-KUMA case, this hyperparameter is fixed at the beginning of the inversion process in a way that the contribution of the regularization term $C_{\underline{m}}(\underline{V})$ corresponds to 9% of the data term $C_{\underline{d}}(\underline{V})$. With such a small initial contribution, the
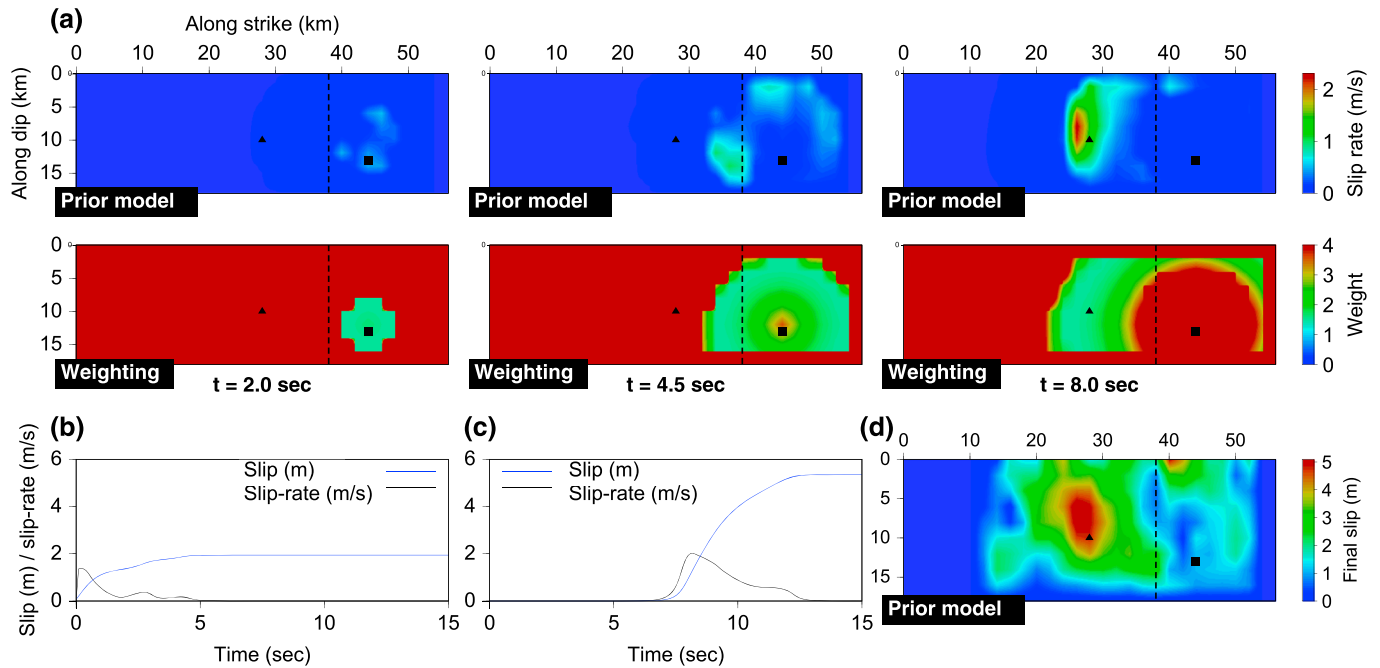
Figure 11. Summary of the prior model, $\underline{V}_p$, and weigthing matrix, $\underline{\underline{W}}_m$, built from the reconstruction and interpretation of the time-space slip inversion from Asano and Iwata (2016). Panel (a) shows evolution of the slip rate distribution (top row) and weighting matrix (bottom row) at three different rupture times ($t = 2.0$, 4.5, and 8.0 s). Panels (b) and (c) illustrate the reconstructed cumulative slip (blue line) and the derived slip rate time histories (black line) at two different fault nodes. Locations of the fault nodes shown in panels (b) and (c) are represented by the black square and triangle on panel (a). The black square represents the hypocentral location, while the triangle illustrates a location near to the zone of expected maximum slip. The vertical black dashed line indicates the division between the Hinagu (shorter) and Futagawa (longer) fault segments. Panel (d) displays final slip distribution of the prior model. In the representation of the weighting matrices shown at the bottom of panel (a), the confidence on the prior model is represented by the colors ranging from blue (low confidence) to red (high confidence).

impact of the regularization is expected to be stronger at the final iterations where most of the data misfit has been already explained. This value of ϵ is defined based on several trials in order to ensure a decent data fit while still taking into account the prior information. On the contrary, for PIS-KUMA case, the hyperparameter ϵ evolves increasingly through the inversion stages. For PIS-KUMA case, the initial contribution of $C_m(\underline{V})$ is set to 2% of $C_d(\underline{V})$ and it increases at each inversion stage to contribute 3% more of the current $C_d(\underline{V})$. For instance, for the second stage of the PIS $\epsilon C_m(\underline{V}) = 0.05 C_d(\underline{V})$, for the third $\epsilon C_m(\underline{V}) = 0.08 C_d(\underline{V})$, and so on. At every step when a new data time window is integrated, the prior model is updated by gathering inversion results of the previous stage. The model weighting matrix is also modified at those nodes where the prior model is replaced, so that any difference between the current model and the modified prior model is strongly penalized. This evolution of the prior model and weighting matrix enforces a causal behavior: it prevents the inversion from modifying the results already obtained to explain the new data, which have more tendency to be mapped into the newly introduced parameters involved in the current inversion stage. That is the reason why the hyperparameter ϵ increases through the PIS procedure. Apart from this difference on the evolution of hyperparameter ϵ, the standard and progressive inversion strategies are carried out under exactly the same time-space discretization and regularization.

The prior model is also used to define the data time windows and their corresponding progressively growing time-space source region to reconstruct. As in the synthetic case, a forward modeling of synthetic seismograms is estimated from the whole prior model history to build a bank of completely recorded seismograms. Then, several forward modelings of time-space limited versions of the prior model are computed to gather the targeted windows of seismograms corresponding to each limited region. Then, we analyze the residuals between the complete seismogram and the selected window to determine the time boundaries of these data windows to be used for each limited source region. PIS-KUMA assumes eight different time windows to be used during the progressive inversion to reconstruct the rupture, expressed as (i.e., 0–1.0, 0–2.0, 0–3.5, 0–5.5, 0–8.0, 0–11.0, 0–15.0, and 0–20.0 s).
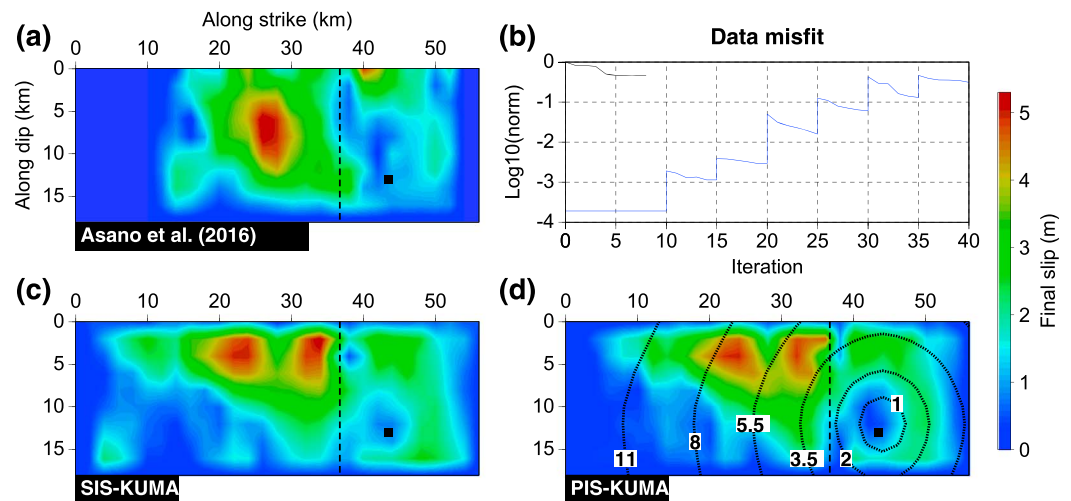
Figure 12. Summary of the results obtained for the 2016 Kumamoto earthquake applying the SIS and the PIS. Panels (a), (c) and (d) show the final slip distributions from the prior model, SIS-KUMA and PIS-KUMA, respectively. Panel (b) shows comparison of the data misfit evolution (L2 norm) of the two inversion strategies. On panels (a), (c), and (d), the vertical black dashed line represents the boundary between the two defined fault segments, while the black square represents the hypocenter location. Both strategies coincide in the overall shape of the final slip. See text for details.

Finally, the depth-dependent and smoothing preconditioning strategies are also set. For setting the optimal value of constant c for the depth-dependent strategy, several inversion exercises are carried out with different c values taking as the inversion target the prior model and without including any regularization. The optimal value of constant c under this configuration is ≈ 0.1. In addition, we consider correlation lengths of 4 km and 3 km along dip and strike, respectively, for smoothing the data gradient at each inversion iteration.

4.3. SIS Versus PIS Real Case

In general, both strategies show similar slip rate evolutions and final slip distributions (see Figure 12). However, results from the SIS present a slightly larger cross talk between the model parameters and longer durations of the rupture at several fault nodes. For instance, the SIS-KUMA final slip distribution (Figure 12c) seems unclear around the hypocentral zone compared to PIS-KUMA (Figure 12d). Furthermore, we recognize a zone of considerably large slip at the northeast bottom of the Futagawa fault segment (bottom left in Figure 12c) that is absent in the PIS-KUMA results. Such result in SIS-KUMA could be caused by the time-space regularization or discretization limits. However, this slip zone is not observed in the PIS-KUMA case, which does not take into account the contribution of these fault nodes until very late inversion stages. The possible influence of this slightly larger cross talk from SIS-KUMA case can be also seen at the higher amplitudes of its final slip distribution compared to the one from the PIS-KUMA (see Figures 12c and 12d). As in the synthetic case, the final slip distribution from the SIS-KUMA case spreads through wider areas on the fault, which could be an expression of the inversion leakage. For instance, results from the PIS-KUMA case exhibit less slip near the hypocenter and at the farthest maximum slip patch while still resolving well enough the seismic moment and the data misfit (Table 3). As a consequence of this behavior, the SIS-KUMA case overestimates the seismic moment (Table 3). On the contrary, results from the PIS2-KUMA seem better spatially constrained around some fault zones and the estimated seismic moment is closer to the one reported by the NIED.

In terms of data misfit, the SIS-KUMA case achieves better results as the final data misfit is 2% less than the misfit from the PIS-KUMA case. However, this better fit of the data might be the consequence of having this wider space-time leakage between nodes. When the SIS-KUMA inversion is performed, more degrees of freedom can be used to fit the data even if strongly penalized. Therefore, the reduction of the data misfit for the SIS-KUMA case is ensured in the least squares sense. The PIS-KUMA case does not fit the data as well as the SIS-KUMA one (34% of data misfit) but the evolution of the number of inverted parameters is rather different. Figure 14 shows a comparison between observed seismograms (solid black line) and inverted seismograms (blue dashed line) for the PIS-KUMA case, corresponding to bottom traces. Top traces (solid black for observed ones and dashed red for synthetic ones) are not used during the inversion and are sufficiently well predicted by the slip rate reconstruction illustrated in Figure 13. While the fit of inverted data is better for SIS-KUMA case

Table 3
Summary of the Results for the SIS and PIS Approaches Applied to the 2016 Kumamoto Mainshock

	$M_0 \times 10^{19}$ [N m]	Final data misfit [%]
NIED	4.42 (M_w 7.06)	
SIS2-KUMA	5.52 (M_w 7.12)	32
PIS2-KUMA	4.86 (M_w 7.09)	34

(not shown in Figure 14), the prediction of traces not used during the inversion for the SIS-KUMA case shows later large oscillations on several recordings. These oscillations lead us to think that the SIS-KUMA inversion overfits the observed data, inducing these spurious oscillations for predictions of unused signals: this is not the case for the PIS-KUMA inversion. Figure 15 illustrates these later oscillations at one of the 11 locations used for waveform prediction: a good quality-control criterion.

It is important to mention that, even if the results from the SIS-KUMA and PIS-KUMA workflows are different, both fit quite well the data and show plausible rupture evolutions. The difference between the SIS-KUMA and PIS-KUMA strategies is one more illustration of the nonuniqueness of the solution, emphasizing the importance of uncertainty quantification in the future. The estimated average rupture speed extracted from the arrival times of the maximum value of the slip rate functions at each node is ≈2.4 km/s. The local values of rake angle that are assumed in this work come from the results from the previous study of Asano and Iwata (2016), and we do not explore the variability of these results with unset rake values. In agreement with these previous studies, the areas that exhibit the maximum slip (≈5.1 m for PIS-KUMA case and ≈5.3 m for SIS-KUMA case)
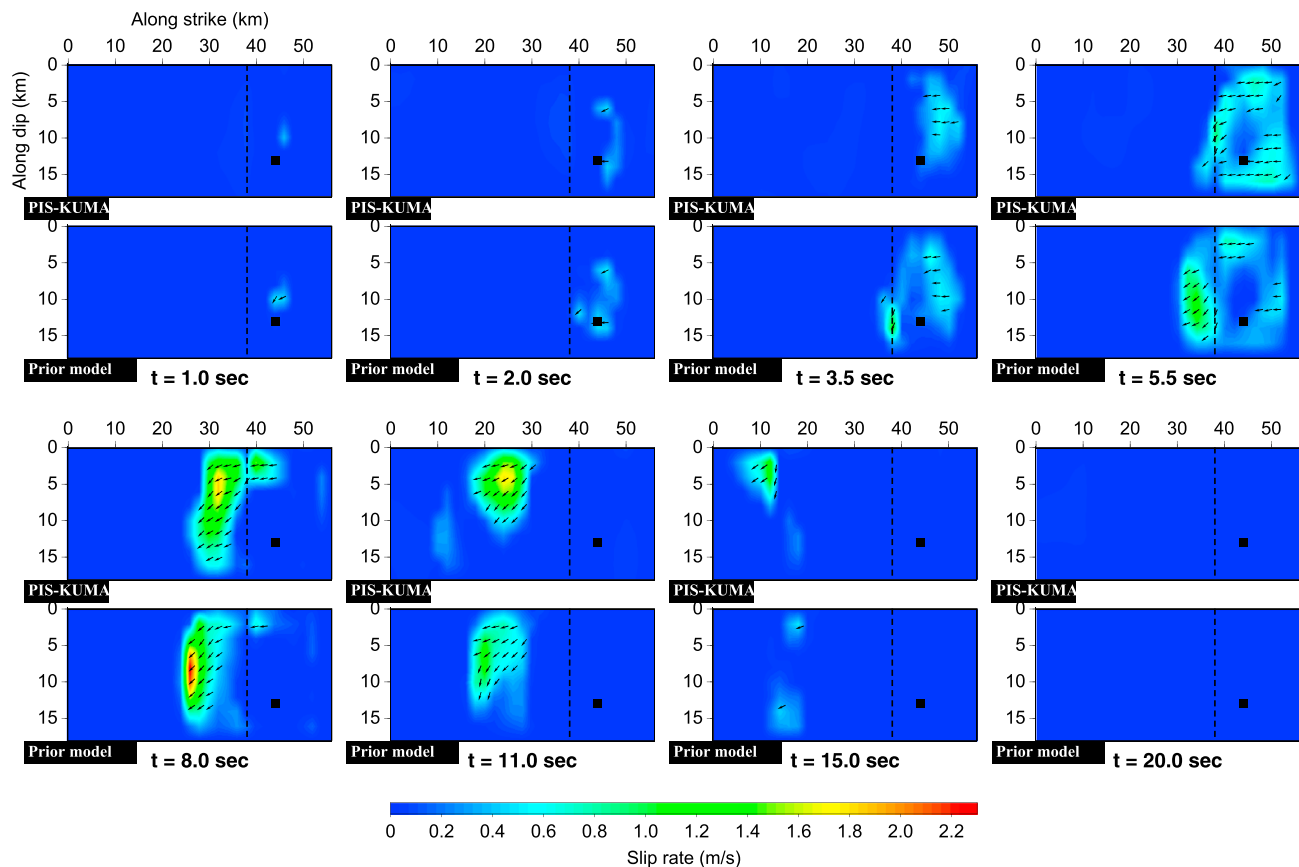

Figure 13. Comparison of the slip rate spatiotemporal distribution obtained from the progressive inversion strategy with regularization (PIS-KUMA) and the prior model. Please note that the solution might differ from the prior model when asked by the data. The time evolution goes from left to right and from top to bottom from 1.0 to 20.0 s. The black square represents the hypocenter location and the dashed vertical black line the boundary between the two fault segments of the assumed fault geometry. Arrows display rake direction of the slip rate vector.
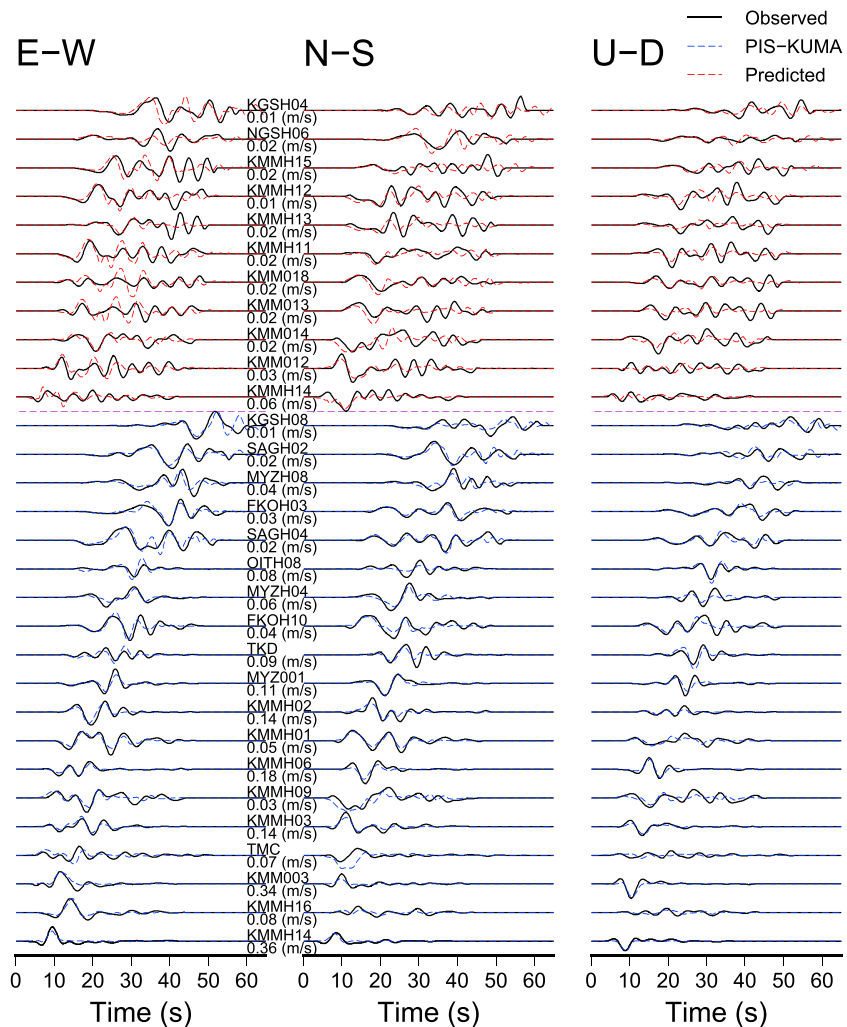
Figure 14. Comparison between observed and synthetic wavefields at 30 stations. Black solid lines represent observed velocity recordings band-pass filtered (0.025–0.25 Hz). Blue and red dashed lines correspond to the synthetic seismograms for stations included in the PIS-KUMA case and for those not included but predicted, respectively. Receiver name and maximum observed velocity at each location are provided next to each E-W trace.

in this study have a small normal component, around 15°-20° from the strike-slip direction, while the other zones exhibit only strike-slip motion. This normal component of the motion at these areas is a coincidence of all the previous studies of this mainshock, and we consider that using this information as a prior information is a pertinent assumption.

According to the PIS-KUMA results, taken as the "best" solution, the rupture initiates on the shortest segment of the fault system. The slip near the hypocenter is considerably less (from 0.2 to 0.9 m) than other shallow regions that exhibited a slip of ≈5 m. The rupture first propagates mostly to the southwest of the Hinagu fault at a low speed around 2.0 km/s (see first three snapshots in Figure 13). After approximately 5 s, the rupture crossed to the Futagawa fault. The rupture across this fault segment propagated from the southwest to the northeast and from deep to shallow zones. The rupture speed accelerated from 2.0 km/s to around 2.6 km/s near the two areas having the maximum slip (≈5.1 m). The rupture does not reach the predefined fault boundaries, with the exception of the upper boundary that exhibits a maximum slip of ≈1.4 m. Once the rupture passes the last area of maximum slip (25 km along strike far from the hypocenter), the rupture speed increased until ≈2.9 km/s (see transitions from snapshots 6 and 7 in Figure 13). This faster speed did not exceed the local shear wave speed of the medium at this region (≈3.2 km/s). However, this increment of the rupture speed could be a consequence of the acceleration that the rupture suffered after breaking the last patch and the lack of resistance to stop the rupture at this farthest region, which could cause a local instantaneous acceleration.
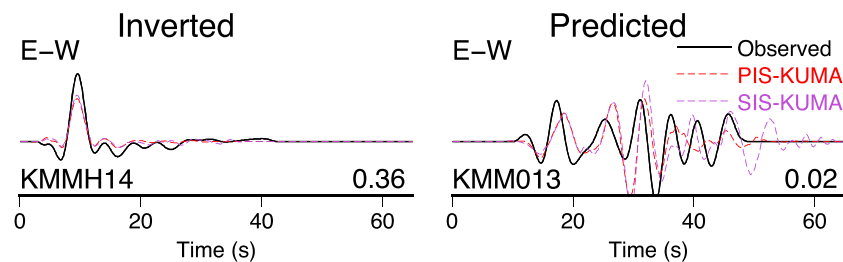
Figure 15. Comparison of observed (solid black line) and synthetic seismograms from slip rate distributions of the SIS-KUMA case (purple dashed line) and the PIS-KUMA case (red dashed line). On the left, the receiver is used in the inversion (similar results in both cases). On the right, the receiver is not used during the inversion but the traces are predicted from the results. SIS-KUMA prediction presents spurious oscillations while the PIS-KUMA one does not. Both traces are E-W components. Receiver name and maximum observed velocity (in m/s) are also provided along the time axis.

As an overall evaluation, the final slip distributions from the SIS-KUMA and PIS-KUMA cases are in agreement with the results from Asano and Iwata (2016), Uchide et al. (2016), and Hao et al. (2017). The hypocentral zone compared to other zones on the fault segments does not provide significant slip contribution. The areas with maximum slip exhibit a normal component of the particle motion. The slip rate propagates from deep to shallow zones and the maximum slip is around 5 to 6 m. However, both solutions show two patches of maximum slip instead of only one as found by others: the diversity of solutions is one key feature of kinematic inversions. The selected fault

geometry and the given velocity structure might have an impact and should be investigated. Nevertheless, we have shown that the evolutive linear kinematic inversion can be applied to real data sets.

5. Discussion and Conclusion

Nowadays, there is a wide variety of strategies to perform a kinematic source inversion. However, to our knowledge, even if most of them are quite fast and efficient, these strategies are using the entire set of records for the investigated event and leave the fitting process to the inversion scheme. In this work, we successfully develop an inverse strategy based on a time domain formulation where the causality feature of the source rupture strongly drives the inversion, mitigating leakage and ambiguity for the reconstruction. By progressively considering increasing time windows at receivers, slip rate is carefully built up on the source surface starting from the hypocenter: Later phases delayed by the propagation kernel will be removed for later slip rate reconstruction. This time domain formulation is based on a linear formulation of the forward problem and an adjoint-state formulation of the optimization. In this inversion, the whole time-space history of the slip rate vector across a 3-D grid representing continuously the source geometry and history is reconstructed. Therefore, the source time function is not assumed at each node but will be reconstructed. In a very flexible and intuitive way, all basic ingredients, such as regularization, prior information and model preconditioning, are introduced in this approach. One may foresee that complex ruptures could be considered for dense acquisition network in the future. Meanwhile, prior information is necessary and is based on expected physical behavior of the seismic rupture. In short, under this linear time domain formulation, the progressive and limited increment of the time-space samples used to invert the source history according to the increasing data time windows reduces the leakage of the information over a large fixed number of time-space samples. This way of handling simultaneously the data and the unknowns reduces the ambiguity or cross talk between neighboring time-space nodes preventing them from representing an equivalent rupture history that, to some extent, fits the data as well as the target solution. With this new hierarchical approach on how to extract information from seismic data for source imaging based on causality, there are two important contributions of this work. The first one is the possibility of performing a partial source reconstruction based on available windows, even before the end of the rupture, opening the door for early warning issues. In other words, by analyzing only the first seconds of a given data set, the nucleation and the beginning of the seismic rupture could be imaged without waiting for the full data set. This strategy has its root in a time formulation, enhancing the explicit causality between rupture and seismograms during the inversion process. This time formulation of slip rate values, related to a wide model space, should be constrained through data-driven and model-driven strategies. Model-driven component injects soft information on how seismic rupture could physically occur

reduces the ill-conditioning of the kinematic reconstruction while still keeping a linear inverse formulation, while alternative reduced-order model strategies in time or in frequency widely used in seismology impose hard constraints on the rupture.

The second main contribution of this work comes with the linearity with respect to model parameters that we have preserved in the forward problem. We have shown that the reconstruction is possible in spite of the drastic increase of unknowns by designing prior models and model covariances (covariance buildup has been kept simple as diagonal matrix but could be improved in the future if needed). This linear property opens road for stochastic inversion in a Bayesian approach which has been recognized as very important for uncertainty quantification in source imaging (Minson et al., 2013). Variabilities of kinematic source reconstruction emphasizes the importance of uncertainty quantification and the need of stochastic inversion for which an evolutive inversion approach based on a forward linear problem is quite appealing.

We have illustrated some of the advantages and performance of this time domain formulation considering a synthetic rupture scenario (SIV1) before inverting real data of the 2016 Kumamoto earthquake (M_w 7.0). The causality introduced into the approach mitigating leakage between parameters leads to different slip amplitude distribution between full time window strategy and increasing time window strategy, even though the overall structure of the slip distribution is recovered for both configurations. Moreover physical plausible regularization terms can be expressed in a natural way without a significant increment of the computational cost or any change in the inverse formulation. Thanks to a precomputed database of the stress-state tensor on a prescribed source geometry, the time domain formulation allows the inversion of progressive data time windows to map restricted space-time regions of the source history. As an evidence of the causality rupture problem, the inversion of very short data time windows provide a satisfactory estimation of the slip rate on the surrounding nucleation zone. Prediction of delayed phases by the propagation operator comes out: further slip rate reconstruction will not consider these already explained quantities. Thus, this progressive strategy opens the door to quasi-real inversions while recording is still occurring.

For standard seismic networks surrounding active faults, physical prior models of the seismic rupture are essential for these time domain formulation: we may have more parameters than unknowns. Nothing prevents us to consider more complex rupture scenarios, especially when more data will be available. Let us mention that the rake attribute extracted from the two slip rate components is poorly constrained by current acquisition design. Therefore, slip rate vector inversion should be cautiously performed in a hierarchical way with prior constraints regarding the variability of the rake angle. In the future, the drastic increase of receivers might reduce this requirement.

References

Aki, K., & Richards, P. G. (2002). *Quantitative seismology theory and methods* (2nd ed.). Sausalito, CA: University Science Books.

Asano, K., & Iwata, T. (2016). Source rupture processes of the foreshock and mainshock in the 2016 Kumamoto earthquake sequence estimated from the kinematic waveform inversion of strong motion data. *Earth, Planets and Space*, *68*(1), 147.

Asnaashari, A., Brossier, R., Garambois, S., Audebert, F., Thore, P., & Virieux, J. (2013). Regularized seismic full waveform inversion with prior model information. *Geophysics*, *78*(2), R25–R36.

Barnhart, W., & Lohman, R. (2010). Automated fault model discretization for inversions for coseismic slip distributions. *Journal of Geophysical Research*, *115*, B10419. https://doi.org/10.1029/2010JB007545

Berteussen, K.-A. (1977). Moho depth determinations based on spectral-ratio analysis of NORSAR long-period P waves. *Physics of the Earth and Planetary Interiors*, *15*(1), 13–27.

Cohee, B. P., & Beroza, G. C. (1994). Slip distribution of the 1992 Landers earthquake and its implications for earthquake source mechanics. *Bulletin of the Seismological Society of America*, *84*, 692–712.

Cotton, F., & Campillo, M. (1995). Frequency domain inversion of strong motions: Application to the 1992 Landers earthquake. *Journal of Geophysical Research*, *100*(B3), 3961–3975. https://doi.org/10.1029/94JB02121

Diao, F., Wang, R., Aochi, H., Walter, T. R., Zhang, Y., Zheng, Y., & Xiong, X. (2016). Rapid kinematic finite-fault inversion for an Mw 7+ scenario earthquake in the Marmara Sea: An uncertainty study. *Geophysical Journal International*, *204*(2), 813–824.

Fan, W., Shearer, P. M., & Gerstoft, P. (2014). Kinematic earthquake rupture inversion in the frequency domain. *Geophysical Journal International*, *199*(2), 1138. https://doi.org/10.1093/gji/ggu319

Fink, M. (1993). Time-reversal mirrors. *Journal of Physics D: Applied Physics*, *26*(9), 1333–1350.

Fink, M. (2008). Time-reversal waves and super resolution. In *Journal of Physics: Conference Series* (Vol. 124(1), 012004 pp.). IOP Publishing.

Gajewski, D., & Tessmer, E. (2005). Reverse modelling for seismic event characterization. *Geophysical Journal International*, *163*(1), 276–284.

Gallovic, F., & Imperatori, W. (2014). Effect of lateral velocity heterogeneities and topography on slip inversions: Case study of the Mw 6.3 2009 L'Aquila earthquake. In *EGU General Assembly Conference Abstracts* (Vol. 16, 2573 pp.).

Hallo, M., & Gallovič, F. (2016). Fast and cheap approximation of Green function uncertainty for waveform-based earthquake source inversions. *Geophysical Journal International*, *207*(2), 1012–1029.

Hansen, P. C. (1992). Analysis of discrete ill-posed problems by means of the L-curve. *SIAM Review*, *34*(4), 561–580.

Hao, J., Ji, C., & Yao, Z. (2017). Slip history of the 2016 Mw 7.0 Kumamoto earthquake: Intraplate rupture in complex tectonic environment. *Geophysical Research Letters*, *44*, 743–750. https://doi.org/10.1002/2016GL071543

Hartzell, S. H., & Heaton, T. H. (1983). Inversion of strong ground motion and teleseismic waveform data for the fault rupture history of the 1979 Imperial Valley, California, earthquake. *Bulletin of the Seismological Society of America*, *73*(6A), 1553–1583.

Haskell, N. (1964). Total energy and energy spectral density of elastic wave radiation from propagating faults. *Bulletin of the Seismological Society of America*, *54*(6A), 1811–1841.

Haskell, N. (1966). Total energy and energy spectral density of elastic wave radiation from propagating faults. Part II. A statistical source model. *Bulletin of the Seismological Society of America*, *56*(1), 125–140.

Heaton, T. H. (1990). Evidence for and implications of self-healing pulses of slip in earthquake rupture. *Physics of the Earth and Planetary Interiors*, *64*(1), 1–20.

Hernandez, B., Cotton, F., & Campillo, M. (1999). Contribution of radar interferometry to a two-step inversion of kinematic process of the 1992 Landers earthquake. *Journal Geophysical Research*, *104*, 13,083–13,099.

Hsieh, M.-C., Zhao, L., Ji, C., & Ma, K.-F. (2016). Efficient inversions for earthquake slip distributions in 3D structures. *Seismological Research Letters*, *87*(6), 1342–1354.

Ide, S. (2007). Slip inversion. In H. Kanamori (Ed.), *Treatise on geophysics* (Vol. 4, pp. 193–223). Amsterdam, Netherlands: Elsevier.

Ide, S., Baltay, A., & Beroza, G. C. (2011). Shallow dynamic overshoot and energetic deep rupture in the 2011 Mw 9.0 Tohoku-Oki earthquake. *Science*, *332*(6036), 1426–1429.

Ishii, M., Shearer, P. M., Houston, H., & Vidale, J. E. (2007). Teleseismic P wave imaging of the 26 December 2004 Sumatra-Andaman and 28 March 2005 Sumatra earthquake ruptures using the Hi-net array. *Journal of Geophysical Research*, *112*, B11307. https://doi.org/10.1029/2006JB004700

Ji, C., Wald, D. J., & Helmberger, D. V. (2002). Source description of the 1999 Hector Mine, California, earthquake, Part I: Wavelet domain inversion theory and resolution analysis. *Bulletin of the Seismological Society of America*, *92*(4), 1192–1207.

Kikuchi, M., & Kanamori, H. (1982). Inversion of complex body waves. *Bulletin of the Seismological Society of America*, *72*(2), 491–506.

Kikuchi, M., & Kanamori, H. (1986). Inversion of complex body waves—II. *Physics of the earth and planetary interiors*, *43*(3), 205–222.

Kikuchi, M., & Kanamori, H. (1991). Inversion of complex body waves—III. *Bulletin of the Seismological Society of America*, *81*(6), 2335–2350.

Kolb, P., Collino, F., & Lailly, P. (1986). Prestack inversion of 1-D medium. In *Extended Abstracts* (Vol. 74, pp. 498–508).

Koper, K. D., Hutko, A. R., Lay, T., Ammon, C. J., & Kanamori, H. (2011). Frequency-dependent rupture process of the 2011 Mw 9.0 Tohoku earthquake: Comparison of short-period P wave backprojection images and broadband seismic rupture models. *Earth, Planets and Space*, *63*(7), 16.

Larmat, C., Montagner, J. P., Fink, M., & Capdeville, Y. (2006). Time-reversal imaging of seimic sources and appplication to the great Sumatra earthquake. *Geophysical Research Letters*, *33*, L19312. https://doi.org/10.1029/2006GL026336.

Lay, T., Ammon, C. J., Kanamori, H., Xue, L., & Kim, M. J. (2011). Possible large near-trench slip during the 2011 M w 9.0 off the Pacific coast of Tohoku earthquake. *Earth, planets and space*, *63*(7), 32.

Liu, P., & Archuleta, R. J. (2004). A new nonlinear finite fault inversion with three-dimensional Green's functions: Application to the 1989 Loma Prieta, California, earthquake. *Journal of Geophysical Research*, *109*, B02318. https://doi.org/10.1029/2003JB002625

Mai, P. M., Schorlemmer, D., Page, M., Ampuero, J.-P., Asano, K., Causse, M., et al. (2016). The earthquake-source inversion validation (SIV) project. *Seismological Research Letters*, *87*, 690–708. https://doi.org/10.1785/0220150231

Minson, S., Simons, M., & Beck, J. (2013). Bayesian inversion for finite fault earthquake source models I—Theory and algorithm. *Geophysical Journal International*, *194*(3), 1701–1726.

Nocedal, J. (1980). Updating quasi-Newton matrices with limited storage. *Mathematics of Computation*, *35*(151), 773–782.

Olson, A. H., & Apsel, R. J. (1982). Finite faults and inverse theory with applications to the 1979 Imperial Valley earthquake. *Bulletin of the Seismological Society of America*, *72*(6A), 1969–2001.

Pérez Solano, C. (2013). Two-dimensional near-surface seismic imaging with surface waves: Alternative methodology for waveform inversion (Ph.D. Thesis), École Nationale Supérieure des Mines de Paris.

Perton, M., Contreras-Zazueta, M. A., & Sánchez-Sesma, F. J. (2016). Indirect boundary element method to simulate elastic wave propagation in piecewise irregular and flat regions. *Geophysical Journal International*, *205*(3), 1832–1842.

Plessix, R. E. (2006). A review of the adjoint-state method for computing the gradient of a functional with geophysical applications. *Geophysical Journal International*, *167*(2), 495–503.

Plessix, R. E., & Mulder, W. A. (2008). Resistivity imaging with controlled-source electromagnetic data: Depth and data weighting. *Inverse Problems*, *24*, 034012.

Podvin, P., & Lecomte, I. (1991). Finite difference computation of traveltimes in very contrasted velocity model: A massively parallel approach and its associated tools. *Geophysical Journal International*, *105*, 271–284.

Satake, K., Fujii, Y., Harada, T., & Namegaya, Y. (2013). Time and space distribution of coseismic slip of the 2011 Tohoku earthquake as inferred from tsunami waveform data. *Bulletin of the Seismological Society of America*, *103*(2B), 1473–1492.

Somala, S. N., Ampuero, J.-P., & Lapusta, N. (2014). *Resolution of rise time in earthquake slip inversions: Effect of station spacing and rupture velocity* (Vol. 104, pp. 2717–2734).

Stein, S., & Wysession, M. (2003). *An introduction to seismology, earthquakes and earth structure*. Malden, MA: Blackwell Publishing.

Suzuki, W., Aoi, S., Sekiguchi, H., & Kunugi, T. (2011). Rupture process of the 2011 Tohoku-Oki mega-thrust earthquake (M9. 0) inverted from strong-motion data. *Geophysical Research Letters*, *38*, L00G16. https://doi.org/10.1029/2011GL049136

Tago, J., Cruz-Atienza, V. M., Virieux, J., Etienne, V., & Sánchez-Sesma, F. J. (2012). A 3D hp-adaptive discontinuous Galerkin method for modelling earthquake dynamics. *Journal of Geophysical Research*, *117*, B09312. https://doi.org/10.1029/2012JB009313

Tinti, E., Fukuyama, E., Piatanesi, A., & Cocco, M. (2005). A kinematic source-time function compatible with earthquake dynamics. *Bulletin of the Seismological Society of America*, *95*(4), 1211–1223.

Uchide, T., Horikawa, H., Nakai, M., Matsushita, R., Shigematsu, N., Ando, R., & Imanishi, K. (2016). The 2016 Kumamoto–Oita earthquake sequence: Aftershock seismicity gap and dynamic triggering in volcanic areas. *Earth, Planets and Space*, *68*(1), 180.

Wald, D. J., & Heaton, T. H. (1994). Spatial and temporal distribution of slip for the 1992 Landers, California, earthquake. *Bulletin of the Seismological Society of America*, *84*, 668–691.

Wald, D. J., Helmberger, D. V., & Hartzell, S. H. (1990). Rupture process of the 1987 Superstition Hills earthquake from the inversion of strong-motion data. *Bulletin of the Seismological Society of America*, *80*(5), 1079–1098.

Zhao, L., Chen, P., & Jordan, T. H. (2006). Strain Green's tensors, reciprocity, and their applications to seismic source and structure studies. *Bulletin of the Seismological Society of America*, *96*(5), 1753–1763.